The Molecular and Electronic Structure of Symmetrically and Asymmetrically Coordinated, Non-Heme Iron Complexes Containing $[Fe^{III}(\mu\text{-}N)Fe^{IV}]^{4+}$ ($S = 3/2$) and $[Fe^{IV}(\mu\text{-}N)Fe^{IV}]^{5+}$ ($S = 0$) Cores

Thomas Jüstel,[a] Michael Müller,[a] Thomas Weyhermüller,[a] Claudia Kressl,[a] Eckhard Bill,[a] Peter Hildebrandt,[a] Marek Lengen,[b] Michael Grodzicki,[b] Alfred X. Trautwein,*[b] Bernhard Nuber,[c] and Karl Wieghardt*[a]

Dedicated to Professor Bernt Krebs on the occasion of his 60th birthday

Abstract: Photolysis of $[LFe^{III}(nadiol)(N_3)]$ (**2**) in dry CH_3CN at 20 °C produces red-brown crystals of the dinuclear *symmetrically* coordinated complex $[\{L(nadiol)Fe\}_2(\mu\text{-}N)]$ (**6**) in 40% yield (L = 1,4,7-trimethyl-1,4,7-triazacyclononane and nadiol^{2-} = naphthaline-2,3-diolate). One-electron oxidation of **6** in dry CH_2Cl_2 with one equivalent of ferrocenium hexafluorophosphate generates blue crystals of $[\{L(nadiol)Fe^{IV}\}_2(\mu\text{-}N)]PF_6$ (**7**). Photolysis of an equimolar CH_3CN solution of $[L(Ph_2acac)Fe^{III}(N_3)]ClO_4$ (**3**) (Ph_2acac^- is the monoanion 1,3-diphenylpropane-1,3-dionate) and $[L(Cl_4\text{-}cat)Fe^{III}(N_3)]$ ($Cl_4\text{-}cat^{2-}$ = tetrachlorocatecholate dianion) produces the *asymmetrically* coordinated species $[L(Ph_2acac)Fe^{III}{=}N{=}Fe^{IV}(Cl_4\text{-}cat)L]ClO_4$ (**8**) in 50% yield. The (μ-oxo)diferric complexes $[\{L(acac)Fe^{III}\}_2(\mu\text{-}O)](ClO_4)_2$ (**4**) (acac$^-$ = pentane-2,4-dionate) and $[\{L(nadiol)Fe^{III}\}_2(\mu\text{-}O)]$ (**5**) have also been prepared for comparison with complexes **6**–**8**. Complexes **4**–**8** have been characterized by single-crystal X-ray crystallography. Complexes **6** and **8** contain mixed-valent $[Fe^{IV}(\mu\text{-}N)Fe^{III}]^{4+}$ cores, whereas **7** contains the linear, symmetric $[Fe^{IV}(\mu\text{-}N)Fe^{IV}]^{5+}$ core with an $Fe^{IV}{-}N_b$ bond length of 1.694(1) Å. The $Fe^{III}{-}N_b$ bond length of 1.785(7) Å in **8** is longer than the $Fe^{IV}{-}N_b$ bond length of 1.695(7) Å at 100 K ($\Delta = 0.09$ Å). The electronic structure of these complexes has been characterized by Mössbauer, electron paramagnetic resonance (EPR), resonance Raman (RR) and UV/Vis spectroscopy, electrochemistry and magnetic susceptibility measurements, and by molecular orbital calculations by local density approximation. These studies reveal that **4** and **5** contain two equivalent high-spin Fe^{III} ions which exhibit the usual antiferromagnetic coupling of the $[Fe^{III}(\mu\text{-}O)Fe^{III}]^{4+}$ core ($J = -90$ and $-95\ cm^{-1}$) to a diamagnetic ground state. Similarly, **7** is diamagnetic even at room temperature and contains two equivalent Fe^{IV} ions, which are strongly antiferromagnetically coupled to also yield an $S = 0$ ground state. On the other hand, complexes **6** and **8** display an $S = 3/2$ ground state and two nonequivalent, strongly antiferromagnetically coupled iron sites with partially delocalized valencies. Therefore, a description of the $[Fe(\mu\text{-}N)Fe]^{4+}$ core as containing a high-spin ferric ion ($S = 5/2$) and a low-spin ferryl ion ($S = 1$) has formal character only.

Keywords: EPR spectroscopy · iron · magnetic properties · Moessbauer spectroscopy · molecular orbital calculations

Introduction

The dinuclear, iron-containing active sites of the non-heme metalloprotein hemerythrin,[1, 2] the R2 subunit of ribonucleotide reductase,[3] methane monooxygenase[4] and other metalloproteins of this kind have been shown to interact in their fully reduced diferrous, catalytically active forms with dioxygen.[5] Reactive intermediates such as hydrogen peroxodiferric, μ-peroxodiferric and high-valent forms containing $[Fe^{III}\text{-}O\text{-}Fe^{IV}]^{5+}$ and $[Fe^{IV}(\mu\text{-}O)_2Fe^{IV}]^{4+}$ cores are subsequently generated.[6] Some of these have been spectroscopically characterized by elaborate techniques such as rapid freeze-quench Mössbauer spectroscopy. Concomitantly with these biochemical or biophysical studies on the biomolecules, a vivid model chemistry has been developed in recent years by Que et al.[7, 8] where the focus is the synthesis of stable dinuclear non-heme complexes containing high-valent Fe^{IV} ions. In general, these species are quite difficult to prepare due to the inherent reactivity toward C–H bonds of these high-valent diiron complexes containing non-heme μ-oxo-

[a] Prof. Dr. K. Wieghardt, Dr. T. Jüstel, Dr. M. Müller, Dr. C. Kressl, Dr. T. Weyhermüller, Dr. E. Bill, Prof. Dr. P. Hildebrandt
Max-Planck-Institut für Strahlenchemie
P.O. Box 10 13 65, D-45413 Mülheim an der Ruhr (Germany)
Fax: (+49) 208-306-3952
E-mail: wieghardt@mpi-muelheim.mpg.de

[b] Prof. Dr. A. X. Trautwein, Dr. M. Lengen, Prof. Dr. M. Grodzicki
Institut für Physik, Medizinische Universität
Ratzeburger Allee 160, D-23538 Lübeck (Germany)

[c] Prof. B. Nuber
Anorganisch-Chemisches Institut der Universität
D-69120 Heidelberg (Germany)

  0947-6539/99/0502-0793 $ 17.50+.50/0

bridged moieties.[9] Model compounds of the above type are very important because they allow the calibration of the spectroscopic tools (e.g. EPR, Mössbauer and EXAFS spectroscopy) on structurally characterized species.

Our approach has been to mellow the enormous reactivity of high-valent μ-oxo-bridged species by replacement of the μ-oxo group by the strongly π-donating μ-nitrido group.[10] Dinuclear (μ-nitrido)diiron complexes with porphinato $(2-)$[11–14] or phthalocyaninato$(2-)$[15, 16] ligands are well known. They contain the linear mixed-valent $[Fe^{3.5}(\mu\text{-}N)Fe^{3.5}]^{4+}$ core. This moiety possesses an EPR-active $S=\frac{1}{2}$ ground state[14] and the Mössbauer spectra, even at 4.2 K, exhibit only a single quadrupole doublet with isomer shifts ranging from $\delta = 0.08$ to 0.18 mm s^{-1}. Accordingly, both iron ions are equivalent and (in spite of the antiferromagnetic coupling between formal low-spin $Fe^{III}(d^5)$ and low-spin $Fe^{IV}(d^4)$ sites) the excess electron is fully delocalized due to strong covalent interactions between Fe and N[14d] so that these complexes belong to class III according to the Robin and Day scheme.[17] Chemically and electrochemically, these complexes can be one-electron oxidized to yield species which contain the diamagnetic $[Fe^{IV}(\mu\text{-}N)Fe^{IV}]^{5+}$ unit; further oxidation to yield coordinated porphyrinate$(1-)$ or phthalocyaninate$(1-)$ π radicals has also been demonstrated.[18] Note that μ-oxo-bridged analogues with $[Fe^{III}(\mu\text{-}O)Fe^{III}]^{4+}$ and $[Fe^{IV}(\mu\text{-}O)Fe^{IV}]^{6+}$ cores which contain porphyrin,[19] phthalocyanine,[20] porphycene,[21] corrole[21] and other ligands[22] of this kind have also been characterized.

In contrast, we have recently discovered that photolysis of mononuclear, non-heme octahedral iron(III) complexes $[LFe^{III}(L')(N_3)]^{n+}$, in which L′ represents a bidentate catecholate dianion $(n=0)$ or acetonylacetonate anion $(n=1)$ derivative in acetonitrile or dichloromethane produces dinuclear, mixed-valent (μ-nitrido)diiron species $[\{L(L')Fe\}_2(\mu\text{-}N)]^{0/1+}$ that contain a $[Fe(\mu\text{-}N)Fe]^{4+}$ core with an $S=\frac{3}{2}$ ground state.[10] Mössbauer spectroscopy established that the valencies are localized in $[\{L(Cl_4\text{-cat})Fe\}_2(\mu\text{-}N)]$.

The X-ray structure determination of this complex[10] showed an interesting feature. Despite the fact that the above neutral molecule possesses crystallographically imposed centrosymmetry in the crystals with the bridging nitrogen located on a crystallographic inversion center, this nitrogen atom appeared to be statically disordered. The successful refinement of the structure with a split atom model with two half-occupied positions for this nitrogen atom on either side of the center of symmetry indicated that the $[Fe(\mu\text{-}N)Fe]^{4+}$ core ($S_t=\frac{3}{2}$) is in fact *asymmetric* with a short Fe–N_b bond at 1.50 Å and a long one at 1.98 Å. It was noted at the time that the accuracy of the determination of these Fe–N_b bond lengths was very low indeed. For the isomorphous, genuinely centrosymmetric complex $[\{L(Cl_4\text{-cat})Fe^{III}\}_2(\mu\text{-}O)]$, no disorder of the bridging oxo group was detected. Furthermore, the non-heme complex $[\{L(Cl_4\text{-cat})Fe^{IV}\}_2(\mu\text{-}N)]Br$ also possesses a genuinely centrosymmetric monocation with a linear, *symmetric* $[Fe^{IV}(\mu\text{-}N)Fe^{IV}]^{5+}$ core ($S=0$) (for ligand abbreviations see Scheme 1).

We decided that the synthesis and full characterization of an *asymmetrically* coordinated species with an $[Fe(\mu\text{-}N)Fe]^{4+}$ core ($S=\frac{3}{2}$) (i.e. possessing two different ligand sets at the two iron ions) would be highly desirable in order to establish the structural and electronic features of this motif. Here we report the preparation, crystal structure and spectroscopic properties of such a species, namely $[L(Ph_2acac)Fe^{III}(\mu\text{-}N)Fe^{IV}(Cl_4\text{-cat})L]ClO_4$. Its ($\mu$-oxo)diferric counterpart $[L(Ph_2acac)Fe^{III}(\mu\text{-}O)Fe^{III}(Cl_4\text{-cat})L]ClO_4$ has recently been described and structurally characterized.[23]

Ligands

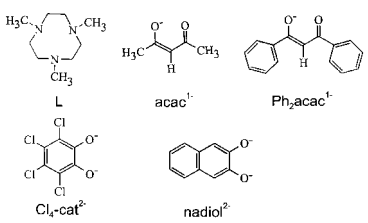

Complexes

$[LFe^{III}(nadiol)Cl]$	**1**
$[LFe^{III}(nadiol)(N_3)]$	**2**
$[LFe^{III}(Ph_2acac)(N_3)]ClO_4$	**3**
$[L(acac)Fe^{III}(\mu\text{-}O)Fe^{III}(acac)L](ClO_4)_2$	**4**
$[L(nadiol)Fe^{III}(\mu\text{-}O)Fe^{III}(nadiol)L]$	**5**
$[L(nadiol)Fe^{III}(\mu\text{-}N)Fe^{IV}(nadiol)L]$	**6**
$[L(nadiol)Fe^{IV}(\mu\text{-}N)Fe^{IV}(nadiol)L]PF_6$	**7**
$[L(Ph_2acac)Fe^{III}(\mu\text{-}N)Fe^{IV}(Cl_4\text{-cat})L]ClO_4$	**8**
$[L(Cl_4\text{-cat})Fe^{III}(\mu\text{-}N)Fe^{IV}(Cl_4\text{-cat})L]$	**9**[10]
$[L(Cl_4\text{-cat})Fe^{III}(\mu\text{-}O)Fe^{III}(Cl_4\text{-cat})L]$	**10**[10]

Scheme 1.

Results

Synthesis of complexes: In the past, we have repeatedly made use of the inherent lability of the chloro ligands in $[LFe^{III}Cl_3]$, two of which are readily displaced by didentate ligands such as acetylacetonates or catecholates. Thus we have prepared $[LFe^{III}(Ph_2acac)Cl]ClO_4$[23] and $[LFe^{III}(Cl_4\text{-cat})Cl]$,[10] both of which are octahedral high-spin iron(III) species. Similarly, the reaction of $[LFeCl_3]$ with naphthaline-2,3-diol in dry methanol in the presence of two equivalents of $Na(OCH_3)$ as auxiliary base affords violet, microcrystalline $[LFe^{III}(nadiol)Cl]$ (**1**) (Scheme 1). In these complexes the remaining chloro ligand is readily substituted by azide to yield the starting materials for the present investigation, namely $[LFe^{III}(nadiol)(N_3)]$ (**2**), $[LFe^{III}(Ph_2acac)(N_3)]ClO_4$ (**3**) and $[LFe^{III}(Cl_4\text{-cat})(N_3)]$.[10] These complexes are also mononuclear octahedral high-spin iron(III) complexes which display a strong $\nu(N_3)$ stretching frequency at 2056 in **2**, 2071 in **3**, and 2069 cm^{-1} in $[LFe(Cl_4\text{-cat})(N_3)]$ in the infrared spectra. This band splits into two at lower frequency upon isotopic labeling with $^{14}N{-}^{14}N{-}^{15}N^-$ (**2**: 2052/2041 and $[LFe(Cl_4\text{-cat})(N_3)]$: 2064/2053 cm^{-1}) where the former corresponds to the $\nu(N_3)$ of the Fe–^{15}N–^{14}N–^{14}N and the latter to the Fe–^{14}N–^{14}N–^{15}N isotopomer. The difference of 11 cm^{-1} for the two isotopomers is indicative of the fact that the two N–N distances in coordinated azides are not equivalent[24] (Δ(N–N) $\approx$ 0.05 Å) as has been shown crystallographically for example in $[(tpp)Fe(N_3)(py)]$ (tpp = tetraphenylporphinate; py = pyridine).[25]

0947-6539/99/0502-0794 $ 17.50+.50/0 *Chem. Eur. J.* **1999**, *5*, No. 2

Complexes which contain the $[Fe^{III}(\mu\text{-}O)Fe^{III}]^{4+}$ core can, in general, be prepared by air oxidation of suitable mononuclear iron(II) complexes or, alternatively, by alkaline hydrolysis of chloroiron(III) species such as **1**, $[LFe^{III}(Cl_4\text{-cat})Cl]$, or $[LFe(Ph_2acac)Cl]ClO_4$ in accordance with Eqation (1) and (2), respectively.

$$2[LFe^{II}(Ph_2acac)Cl]+\tfrac{1}{2}O_2 \xrightarrow{CH_3CN} [\{LFe^{III}(Ph_2acac)\}_2(\mu\text{-}O)]^{2+}+2Cl^- \quad (1)$$

$$2[LFe^{III}(nadiol)Cl]+2OH^- \xrightarrow{acetone} [\{LFe^{III}(nadiol)\}_2(\mu\text{-}O)]+H_2O+2Cl^- \quad (2)$$

We have synthesized $[\{LFe(acac)\}_2(\mu\text{-}O)](ClO_4)_2$ (**4**) as yellow-brown crystals from the reaction of $[Fe(acac)_3]$ with L in acetone containing a small amount of water with addition of $NaClO_4$. Hydrolysis of **1** in acetone with 0.10 M aqueous NaOH yields $[\{LFe^{III}(nadiol)\}_2(\mu\text{-}O)]$ (**5**). The reaction [Eq. (2)] has also been shown[23] to produce an asymmetrically coordinated (μ-oxo)diferric species when an equimolar mixture of two different mononuclear chloro complexes, for example $[LFe^{III}(Ph_2acac)Cl]ClO_4$ and $[LFe^{III}(Cl_4\text{-cat})Cl]$, is hydrolyzed. From this reaction, the symmetric complexes $[\{LFe^{III}(Cl_4\text{-cat})\}_2(\mu\text{-}O)]$ (**10**) and $[\{LFe^{III}(Ph_2acac)\}_2(\mu\text{-}O)](ClO_4)_2$ and the *asymmetric* species $[L(Ph_2acac)Fe^{III}\text{-}O\text{-}Fe^{III}(Cl_4\text{-cat})L]ClO_4$ were isolated in ≈30% yield, respectively.

When deep red microcrystalline $[LFe(Ph_2acac)(N_3)]BPh_4$ was heated to 190 °C in a dynamic vacuum for ≈15 minutes, a color change to deep blue was observed. Differential thermal analysis and thermogravimetric experiments of this process revealed that 1.4 ± 0.2 equivalents of N_2 per equivalent of $[LFe^{III}(Ph_2acac)(N_3)]BPh_4$ are produced at 174.8 °C in a single exothermic step. In the infrared spectrum of the resulting material, no $\nu(N_3)$ stretching frequency is observed. From the Mössbauer spectrum and magnetic susceptibility measurements (see below) it is evident that a high-spin iron(II) species $[LFe^{II}(Ph_2acac)](BPh_4)$ is formed as shown in Equation (3).

$$[LFe^{III}(Ph_2acac)(N_3)]^+ \xrightarrow{\Delta H} [LFe^{II}(Ph_2acac)]^+ + 1.5\,N_2 \quad (3)$$

Presumably, $[LFe^{II}(Ph_2acac)]^+$ is five-coordinate. Mechanistically, this implies that in the rate-determining step, homolysis of the Fe^{III}–N_3 bond takes place with formation of the iron(II) species and an $N_3\cdot$ radical which decomposes rapidly to dinitrogen. In acetonitrile, this complex reacts rapidly with O_2 with quantitative formation of $[L(Ph_2acac)\text{-}Fe^{III}\text{-}O\text{-}Fe^{III}(Ph_2acac)L](BPh_4)_2$ which has previously been structurally characterized.[23]

Photolysis of a solution of $[LFe(Cl_4\text{-cat})(N_3)]$ in anhydrous, argon-purged acetonitrile at 0 °C with a quartz Hg immersion lamp (254 – 400 nm) has been shown to produce the dinuclear, symmetric μ-nitrido complex $[L(Cl_4\text{-cat})Fe^{III}(\mu\text{-}N)Fe^{IV}(Cl_4\text{-cat})L]$ (**9**) in 42% yield (based on the starting material) and the mononuclear species $[LFe^{II}(Cl_4\text{-cat})(NCCH_3)]\cdot 2H_2O$ in 40% recovered yield.[10] In an analogous photolysis reaction of **2**, the symmetric complex $[\{L(nadiol)Fe\}_2(\mu\text{-}N)]$ (**6**) was obtained in 41% recovered yield. Depending on the residual oxygen and moisture in the solvent employed, the (μ-nitrido)diiron complexes are, in general, contaminated by the corresponding (μ-oxo)diferric complexes, such as **10** and **5**.

Bromine and ferrocenium hexafluorophosphate oxidation of $[\{L(Cl_4\text{-cat})Fe\}_2(\mu\text{-}N)]$ and **6**, respectively, in dry CH_2Cl_2 affords black-green crystals of $[\{L(Cl_4\text{-cat})Fe^{IV}\}_2(\mu\text{-}N)]Br$[10] and blue crystals of $[\{L(nadiol)Fe^{IV}\}_2(\mu\text{-}N)]PF_6$ (**7**). Both complexes are diamagnetic even at room temperature (^1H NMR spectroscopy). Since the corresponding neutral (μ-oxo)diferric species do not react with these oxidants, they remain in solution after precipitation of the above salts. Subsequent reduction of $[\{L(Cl_4\text{-cat})Fe^{IV}\}_2(\mu\text{-}N)]Br$ and **7** in acetonitrile with $N_2H_4\cdot H_2O$ yields the pure mixed-valent (μ-nitrido)diiron species. This procedure is therefore suitable for the preparation of (μ-oxo)diferric-free samples.

Photolysis of an equimolar solution of two different azidoiron(III) complexes, namely $[LFe^{III}(Cl_4\text{-cat})(N_3)]$ and **3**, in dry acetonitrile produced a deep brown solution from which the asymmetric species $[L(Ph_2acac)Fe(\mu\text{-}N)Fe(Cl_4\text{-cat})L]ClO_4$ (**8**) was obtained as brown-black crystals in ≈50% yield based on the total iron content. Interestingly, we did not find any evidence for the formation of the *symmetric* analogues $[\{L(Ph_2acac)Fe\}_2(\mu\text{-}N)]^{2+}$ or **9** in the above reaction. This is an important observation since photolysis under identical reaction conditions of $[L(Cl_4\text{-cat})Fe^{III}(N_3)]$ is known to produce **9** in 42% yield (see above). The mechanistic implications will be discussed later.

Electrochemistry: The electrochemistry of complexes has been studied by cyclic voltammetry and controlled potential coulometry on acetonitrile, dichloromethane or acetone solutions which contained 0.10 M tetra-*n*-butylammonium hexafluorophosphate as supporting electrolyte at a glassy carbon working electrode. All potentials are referenced in volts with reference to the ferrocenium/ferrocene (Fc^+/Fc) couple. The results are given in Table 1.

Table 1. Redox potentials of complexes.[a]

Complex	E [V] vs Fc^+/Fc[b]			Solvent[c]
1	+0.34(irr)		−1.15(irr)	acetone
2	+0.36(irr)		−1.15(irr)	CH_3CN
3	+1.11(irr)	−0.50(r)		CH_3CN
4			−1.04(r)	CH_3CN
5	+0.03(irr)		−1.58(r)	CH_3CN
6, **7**		−0.67(r)	−1.41(r)	CH_3CN
8	+0.75(r) 0.02(q. r.)		−1.01(r)	CH_3CN
$[L(Cl_4\text{-cat})FeCl]$	+0.43(r)		−1.07(r)	CH_2Cl_2
$[L(Cl_4\text{-cat})Fe(N_3)]$	+0.43(r)		−1.07(r)	CH_2Cl_2
9	+0.55(r)	−0.61(r)		CH_2Cl_2
10	+0.44(r)	+0.20(r)	−1.69(r)	CH_2Cl_2

[a] Conditions: glassy carbon working electrode, scan rate 100 mV s^{-1}. [b] For reversible (r) processes redox potentials $E_{1/2} = (E_{p,a} + E_{p,c})/2$ and for irreversible (irr) processes peak potentials $E_{p,a}$ or $E_{p,c}$ are given. [c] 0.10 M $[(n\text{Bu})_4N]PF_6$ supporting electrolyte.

The cyclic voltammograms of the mononuclear complexes **1** and **2** display two irreversible processes at very cathodic (reduction of $Fe^{III} \rightarrow Fe^{II}$) and at an anodic potential which involves a ligand-centered oxidation (catecholate$(2-) \rightarrow$ sequinonate$(1-)$). For **3**, the reduction is reversible at a less cathodic potential but the irreversible ligand-centered oxidation occurs at a much more positive potential. For $[L(Cl_4\text{-}$

cat)FeCl] and [L(Cl_4-cat)Fe(N_3)], both the metal reduction and the ligand oxidation are reversible. From these results it is clearly established that coordinated catecholates stabilize the Fe^{III} oxidation state by $\approx$500 mV compared to their β-diketonate(1 $-$) analogues. Conversely, coordinated catecholates are more easily oxidized than β-diketonates by $\approx$600 mV.[23]

The (μ-oxo)diferric complexes **4**, **5**, and **10** each display a reversible one-electron reduction at negative potentials generating mixed-valent complexes with a $[Fe^{II}(\mu\text{-}O)Fe^{III}]^{3+}$ core. Note that $[\{L(Ph_2acac)Fe\}_2(\mu\text{-}O)]BPh_4$ with an $[Fe^{II}(\mu\text{-}O)Fe^{III}]^{3+}$ core has been isolated and characterized by X-ray crystallography as a mixed-valent class II species with an $S = ½$ ground state.[26] The redox potential for the latter species has been reported at -0.97 V. The irreversible oxidation of **5** at 0.03 V is again a ligand-centered process which, in **10**, is reversible at $E_{1/2} = +0.20$ V. The latter also shows a second reversible oxidation wave at 0.44 V which is presumably also a ligand-centered oxidation of a coordinated catecholate $\rightarrow$semiquinonate.[23]

The cyclic voltammograms of **6** and **7** are identical and display two reversible one-electron transfer waves at $E_{1/2}$ values of -0.67 and -1.41 V. From coulometry at -0.50 V, it is established that the first process corresponds to a one-electron oxidation of **6** to generate **7** with a $[Fe^{IV}(\mu\text{-}N)Fe^{IV}]^{5+}$ core. The second process is a one-electron reduction, showing that the $[Fe^{III}(\mu\text{-}N)Fe^{III}]^{3+}$ core is at least electrochemically accessible albeit at a very negative potential. Interestingly, both processes are also observed in the cyclic voltammogram of the asymmetrically coordinated species **8** but the $[Fe(\mu\text{-}N)Fe]^{4+}$ core is more difficult to oxidize to the $[Fe^{IV}(\mu\text{-}N)Fe^{IV}]^{5+}$ unit by 690 mV and more easily reduced to the $[Fe^{III}(\mu\text{-}N)Fe^{III}]^{3+}$ core by 400 mV. Evidently, binding of one β-diketonate ligand in **8** instead of two catecholates as in **6** and **9** reduces the accessibility of the highest metal-centered oxidation level, $[Fe^{IV}(\mu\text{-}N)Fe^{IV}]^{5+}$, and makes the reduced form $[Fe^{III}(\mu\text{-}N)Fe^{III}]^{3+}$ more readily accessible. Note that all complexes containing a tetrachlorocatecholate ligand display reversible ligand-centered oxidation to generate a coordinated tetrachlorosemiquinonate. Thus [L(Ph_2acac)$Fe^{III}(\mu$-O)-Fe^{III}(Cl_4-semiquinonate)L]-(ClO_4)(BF_4) has been isolated and characterized by Mössbauer spectroscopy.[23]

Crystal structures: The structures of **4**·toluene, **5**·2 mesitylene, **6**·2 toluene, **7**·toluene, and **8**·toluene have been determined by single-crystal X-ray crystallography. Figure 1 shows the structure of the dication in crystals of **4**, Figure 2 those of the neutral molecules in **5**, **6**, and the monocation in **7**, and Figure 3 that of the monocation in **8**. Important structur-

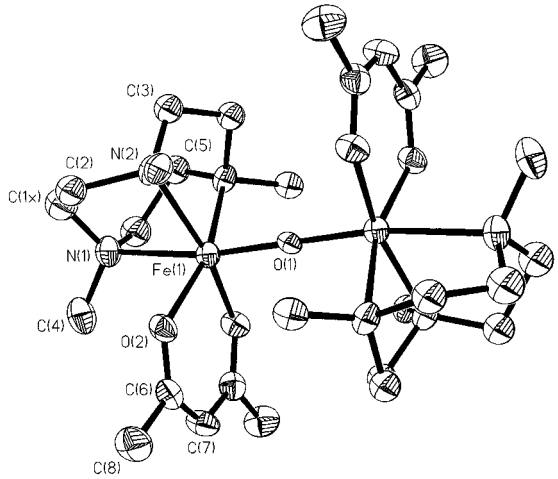

Figure 1. Perspective view of the dication in the crystal structure of **4**·toluene. Hydrogen atoms are omitted for clarity.

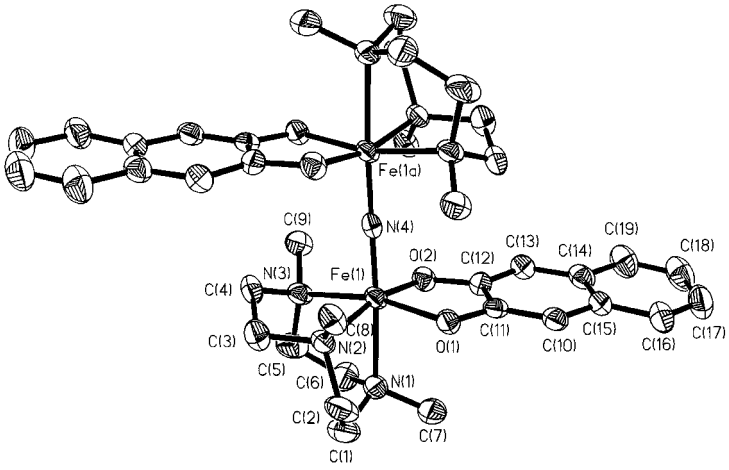

Figure 2. Perspective view of the neutral molecule in the crystal structure of **6**·2 toluene. Hydrogen atoms are omitted for clarity. The structure of the (μ-oxo)diferric analogue in **5**·2 mesitylene is very similar and is not shown. The structure of the monocation in **7**·1 toluene is also very similar and not shown.

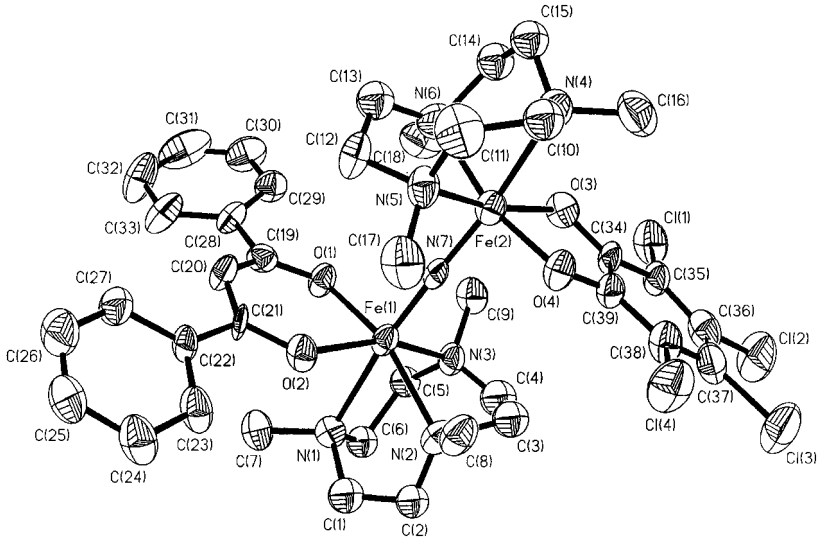

Figure 3. Perspective view of the asymmetrically coordinated monocation in the crystal structure of **8**·1 toluene (295 K).

0947-6539/99/0502-0796 $ 17.50+.50/0 *Chem. Eur. J.* **1999**, *5*, No. 2

Table 2. Selected bond lengths and angles of complexes.

Complex	Fe – X_b [Å][a]	Fe – N_{trans} [Å][b]	av. Fe – N_{cis} [Å][b]	av. Fe – O, [Å][c]	Fe-X_b-Fe [°]	T [K]
4	1.806(2)	2.330(9)	2.184(6)	2.001(5)	180	293
5	1.799(1)	2.367(5)	2.220(6)	1.982(4)	180	293
6	1.95(2)/1.54(2)	2.360(8)	2.166(9)	1.955(7)	180	293
7	1.694(1)	2.199(5)	2.052(6)	1.901(4)	180	293
8[d]	1.785(7)	2.403(7)	2.206(6)	2.046(5)	178.6(4)	100
	1.695(7)	2.229(7)	2.057(7)	1.922(5)		
[{L(Ph_2acac)Fe^{III}}(μ-O)-	1.787(3)	2.337(4)	2.190(4)	2.015(3)	173.7(2)	293
{Fe^{III}(Cl_4-cat)}L]BPh_4[e]	1.825(3)	2.354(4)	2.204(4)	1.980(3)		

[a] Average bond length Fe – O_b or Fe – N_b of the bridging Fe-O_b-Fe or Fe-N_b-Fe unit. [b] Fe – N bond lengths of the coordinated cyclic triamine. N_{trans} is in *trans* and two N_{cis} atoms are in *cis* position relative to the Fe – X_b bond. [c] Average Fe – O bond length of coordinated acetonylacetato or catecholato ligands. [d] The upper first average value refers to bond lengths in the {LFe(Ph_2acac)} half and the lower second one to those in the {LFe(Cl_4-cat)} half of the asymmetric complex. [e] Ref. [23].

al data of the first coordination spheres only are summarized in Table 2.

The structures of the (μ-oxo)diferric complexes in **4** and **5** consist of two octahedral iron(III) ions each coordinated to a cyclic triamine L and a bidentate chelate $acac^-$ or $nadiol^{2-}$ ligand which are bridged by an oxo group. Both dinuclear complexes possess crystallographically imposed symmetry (at least C_i) where the bridging oxygen lies on a crystallographic center of symmetry. Consequently, the Fe(μ-O)Fe moiety is linear in both cases. In contrast, in the analogous dication in [(tacn)(acac)Fe^{III}(μ-O)Fe^{III}(acac)(tacn)]$(ClO_4)_2$, this unit is significantly bent at 158.6(3)° (tacn = 1,4,7-triazacyclononane, the unmethylated derivative of L).[27] As usual, the Fe–O_{oxo} bonds are short and display considerable double-bond character and they exert a significant structural *trans* influence on the Fe–N_{trans} bond in *trans* position relative to the Fe–O_{oxo} bond. Thus the difference between the Fe–N_{trans} and the average Fe–N_{cis} bond, Δ[(Fe–N_{trans}) – (Fe–N_{cis})], is 0.146 Å in **4** and **5**.

Compounds **6** and **7** consist of dinuclear species that contain the [Fe(μ-N)Fe]$^{4+}$ and the [Fe(μ-N)Fe]$^{5+}$ core, respectively. Each iron center is coordinated to a cyclic triamine L and a bidentate naphthaline-2,3-diolate(2 –) ligand. In both structures, the bridging nitride lies on a crystallographic center of symmetry. Careful examination of the distribution of the total and residual electron density in the two Fe(μ-N)Fe structural units reveals that this unit is linear and symmetric in **7** only. In contrast, for **6**, it was possible to calculate (and refine) two statically disordered positions at either side of the crystallographic center of symmetry for the bridging nitrogen with a split-atom model. This implies that the [Fe(μ-N)Fe]$^{4+}$ unit in **6** is in fact asymmetric, with a short Fe–N bond of 1.54(2) Å and a longer one at 1.95(2) Å. The accuracy of these distances is low. Due to this disorder phenomenon in **6**, the Fe–N and Fe–O bond lengths given in Table 2 represent only the averaged values of the LFe^{III}(nadiol) and LFe^{IV}(nadiol) unit. In **7** this problem is not encountered; here the [Fe(μ-N)Fe]$^{5+}$ unit is symmetric and the Fe–N_b distance at 1.694(1) Å is short and displays considerable double-bond character. Very similar behavior has been reported by us for the complexes [{L(Cl_4-cat)Fe}$_2$(μ-N)] and [{L(Cl_4-cat)-Fe^{IV}}$_2$(μ-N)]Br.[10]

It is noteworthy that the C–O and C–C bond lengths of the bound $nadiol^{2-}$ and Cl_4-cat^{2-} ligands in **5**–**8** are identical within experimental error, which indicates catecholate rather than semiquinonate binding. A comparison of the average Fe–O_{nadiol} and Fe–N_{cis} distances in **5**–**7** reveals a monotonic decrease of these bond lengths with increasing oxidation state of the central iron ion ranging from +III in **5**, partially delocalized between III and IV in **6**, to +IV in **7**. This effect is largely due to the differing electronic configurations of the iron ions: in the [LFe^{III}(nadiol)]$^+$ unit of **5** a high-spin configuration ($S = 5/2$) with two half-filled e_g^* orbitals is present, whereas in the [LFe^{IV}(nadiol)]$^{2+}$ unit of **7** a low-spin configuration ($S = 1$) with *empty* e_g^* orbitals prevails. The nitrido bridge in **7** exerts a substantial structural *trans* influence on the Fe–N_{trans} bond. Thus Δ[(Fe–N_{trans}) – (Fe–N_{cis})] is 0.147 Å.

Crystals of **8** contain the *asymmetrically* coordinated monocation [L(Ph_2acac)Fe^{III}(μ-N)Fe^{IV}(Cl_4-cat)L]$^+$ where one L(Ph_2acac)Fe fragment is bound by a nitrido bridge to an LFe(Cl_4-cat) unit. Naturally, the two halves are not related to each other by a crystallographic symmetry element. As already indicated above, the average Fe–N_{cis} bond lengths of the cyclic amine L can be used as a marker for the oxidation state of the iron center to which it is bound.[23] The octahedral [LFe(O,O′-chelate)X] fragment has been characterized for complexes which contain Fe^{II} (d^6 high-spin), Fe^{III} (d^5 high-spin), and Fe^{IV} (d^4 low-spin), where the average Fe–N_{cis} distance was found to be 2.25, 2.18, and 2.05 Å, respectively. It is then immediately evident that the LFe^{III}(Ph_2acac) fragment in **8** contains a trivalent iron center and LFe^{IV}(Cl_4-cat) contains a tetravalent iron center because the average Fe–N_{cis} distance for the former is 2.21 Å and 2.06 Å for the latter. The difference of 0.15 Å for the same type of bond is indicative of an oxidation state difference of one. This interpretation is corroborated by the observation that the two Fe–N_b distances in the mixed-valent [Fe(μ-N)Fe]$^{4+}$ core of **8** are also significantly different: a short Fe^{IV}–N_b bond at 1.695(7) Å and a longer Fe^{III}–N_b bond at 1.785(7) Å are observed ($\Delta = 0.090$ Å).

On the other hand, the value for Δ of 0.090 Å is not as large as one might have anticipated if the asymmetric resonance structure [Fe^{III}–N≡Fe^{IV}]$^{4+}$ would play a significant role. In this case, a more symmetric resonance structure seems to describe the bonding more appropriately since Δ reflects predominantly the difference of the effective ionic radii of an octahedral high-spin Fe^{III} and a low-spin Fe^{IV} ion which is ≈0.06 Å. Note that the observed Fe–N_b distance of

1.694(1) Å in **7** with a symmetric $[Fe^{IV}(\mu\text{-}N)Fe^{IV}]^{5+}$ core is equidistant with the short $Fe-N_b$ bond in **8**.

Vibrational spectroscopy: The resonance Raman (RR) and infrared spectral properties of the compounds studied are listed in Table 3. The asymmetric and symmetric stretching modes, ν_{as} and ν_s, of the $[Fe(\mu\text{-}O)Fe]^{4+}$ core in **10** have been observed in the infrared and resonance Raman spectrum,

Table 3. Vibrational data of dinuclear complexes.

Complex	ν_{as}(Fe-X-Fe) [cm^{-1}]	ν_s(Fe-X-Fe) [cm^{-1}]	Ref.
10	817 (IR) 776 (IR)[a]	354 (RR) 354 (RR)[a]	[10], this work
5	806 (IR)	362 (RR)	this work
[{L(Ph_2acac)Fe}(μ-O)-{Fe(Cl_4-cat)L}]ClO_4	802 (IR)		[23]
9	911(RR) 884(RR)[b]	n. o.	[10]
6	918(RR) 891(RR)[b]	n. o.	this work
[{L(Cl_4-cat)Fe}$_2$(μ-N)]Br	n. o.	414 (RR)	[10]

[a] Fe-^{18}O-Fe isotopomer. [b] Fe-^{15}N-Fe isotopomer. IR: infrared spectrum; RR: resonance Raman spectrum; n.o.: not observed.

respectively, and have been unequivocally assigned by their ^{18}O shifts, which are -41 cm^{-1} for the ν_{as}(Fe-O-Fe) and 0 cm^{-1} for the ν_s(Fe-O-Fe). These values are characteristic for a linear $[Fe^{III}(\mu\text{-}O)Fe^{III}]^{4+}$ moiety.[28] Figure 4 shows the RR spectra of this complex recorded at two different excitation

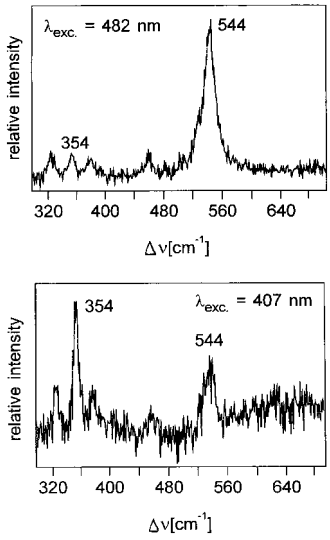

Figure 4. RR spectra of **10** in acetone at 295 K at $\lambda_{exc} = 482$ nm (top) and 407 nm (bottom).

frequencies, 482 and 407 nm, the former of which coincides with a catecholate-to-iron charge transfer (CT) band at 491 nm ($\varepsilon = 5.0 \times 10^3$ $Lmol^{-1}cm^{-1}$) and the latter is in the region where oxo-to-iron CT bands are observed.[29] Consequently, the most intense band at 544 cm^{-1} observed with excitation at 482 nm is assigned to the $\nu(Fe-O_{cat})$ stretching frequency, whereas the most prominent band at 354 cm^{-1} ($\lambda_{exc} = 407$ nm) is the ν_s(Fe-O-Fe). Similar results have been obtained for **5**. It should be pointed out that the ν_{as}(Fe-O-Fe) stretch has been readily identified as a relatively strong band in the infrared spectrum for all complexes which contain a $[Fe(\mu\text{-}O)Fe]^{4+}$ core in the present study and for those reported in the literature. This is also the case for the ν_s(Fe-O-Fe) band in the RR spectrum upon appropriate excitation into the $[Fe(\mu\text{-}O)Fe]^{4+}$ CT absorption maximum.[28]

According to Sanders-Loehr et al.[28] there is a correlation between $\Delta(\nu_{as} - \nu_s)$ and the bridging Fe-O-Fe angle α: Δ is 450–500 cm^{-1} for species with a linear Fe-O-Fe core ($\alpha = 180^o$) and ≈ 200 cm^{-1} when $\alpha = 120^o$. In the present study Δ is 463 cm^{-1} for **10**, and 444 cm^{-1} for **5** in good agreement with the fact that both species have a linear Fe-O-Fe core.

The situation appears to be more complicated for complexes containing the symmetric, linear $[Fe^{IV}(\mu\text{-}N)Fe^{IV}]^{5+}$ ($S = 0$) core, the symmetric, linear $[Fe^{3.5}(\mu\text{-}N)Fe^{3.5}]^{4+}$ ($S = ½$), and the asymmetric $[Fe^{III}(\mu\text{-}N)Fe^{IV}]^{4+}$ ($S = ³⁄₂$) core. In order to allow the unambiguous detection of the vibrational modes of these cores we have synthesized the complexes [{L(Cl_4-cat)Fe}$_2$(μ-N)], [{L(Cl_4-cat)-Fe}$_2$(μ-N)]Br, and **6** with ^{15}N labeled azide, ^{15}N-^{14}N-$^{14}N^-$, which gives rise to two isotopomers $[Fe(\mu\text{-}^{15}N)Fe]^{4+}$ and $[Fe(\mu\text{-}^{14}N)Fe]^{4+}$ in a 1:1 ratio.

It is somewhat surprising and unexpected that the ν_{as}(Fe-N-Fe) stretch has not been observed in the infrared spectra of **6**, **7**, asymmetric **8** and the above two tetrachlorocatecholate-derived, symmetric μ-nitrido complexes with $[Fe(\mu\text{-}N)Fe]^{4+/5+}$ cores. For at present unknown reasons the intensity of this mode appears to be very small in the infrared spectrum. In contrast, the ν_{as} mode has been detected in the RR spectra ($\lambda_{exc} = 413$ nm) of [{L(Cl_4-cat)Fe}$_2$(μ-N)] (Figure 5) but the expected ν_s mode has *not* been observed. Similar results have been obtained for **6**. Note that both complexes contain the asymmetric $[Fe(\mu\text{-}N)Fe]^{4+}$ core with two nonequivalent iron sites. For both compounds, isotopic labeling with ^{15}N leads to a shift of ≈ 27 cm^{-1} to lower energy for the ν_{as}(Fe-N-Fe) stretch. The model for a simple two-atom harmonic Fe≡N oscillator predicts this shift to be 25 cm^{-1}.

For complexes that contain the symmetric, linear $[Fe(\mu\text{-}N)Fe]^{5+}$ core as in [{L(Cl_4-cat)Fe^{IV}}$_2$(μ-N)]Br, the situation is again different: neither the ν_{as}(Fe-N-Fe) nor the ν_s(Fe-N-Fe) band is detected in the infrared spectrum, but in the RR spectrum the latter is observed at 414 cm^{-1}, whereas the ν_{as}(Fe-N-Fe) mode is now *not* detected. Both isotopomers display the ν_s(Fe-N-Fe) at 414 cm^{-1} as the most prominent band ($\lambda_{ecx} = 407$ nm); there is no isotope shift as expected for a linear, symmetric [Fe-N-Fe]$^{5+}$ core.

Similar problems have evidently been encountered by authors who describe the vibrational spectroscopy of [{(tpp)Fe}$_2$(μ-N)]ClO_4[30] and [{(pc)Fe}$_2$(μ-N)]PF_6[15d] (Table 4). For the former a ν_{as}(Fe-N-Fe) mode has been assigned to a vibration observed in the infrared spectrum at 1000 cm^{-1} but isotopic labeling by ^{15}N did not change its position. Therefore, this assignment is probably not correct. In the RR spectrum the ν_s(Fe-N-Fe) mode has been identified at 465 cm^{-1}. In the latter phthalocyaninato complex, no vibrations of the $[Fe(\mu\text{-}N)Fe]^{5+}$ core were found in the infrared spectrum.[15d] Interestingly, in the corresponding porphyrinato and phthalocyaninato μ-carbido complexes the ν_{as}(Fe-C-Fe) is detected in the infrared and the ν_s(Fe-C-Fe) in the RR spectrum (Table 4).[30, 31]

0947-6539/99/0502-0798 $ 17.50+.50/0 *Chem. Eur. J.* **1999**, *5*, No. 2

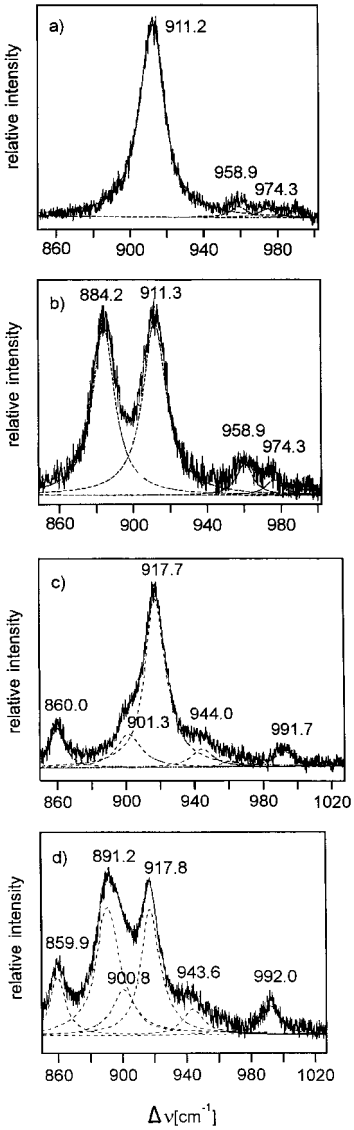

Figure 5. RR spectra of **9** (a,b) and **6** (c,d) at $\lambda_{exc} = 413$ nm in CH_3CN. Spectra b) and d) are those of the corresponding $^{14}N/^{15}N$ isotopomers (1:1). Dotted lines represent band fits.

Table 4. Vibrational spectroscopy of μ-oxo, μ-nitrido-, and μ-carbido bis(tetraphenylporphinato)diiron and bis(phthalocyaninato)diiron complexes.

Complex	ν_{as}(Fe-X-Fe) [cm^{-1}]	ν_s(Fe-X-Fe) [cm^{-1}]	Ref.
[(tpp)$_2$Fe$_2$(μ-N)]	885, 910(IR)	424 (RR)	[34]
[(pc)$_2$Fe$_2$(μ-N)]	915 (IR)	n. r.	[15a]
[(tpp)Fe(μ-N)Fe(pc)]	930 (IR)	n. r.	[16a]
[(tpp)$_2$Fe$_2$(μ-N)](ClO$_4$)	1000(?) (IR)	465 (RR)	[30]
[(tpp)$_2$Fe$_2$(μ-C)]	946 (IR)	440 (RR)	[30]
(pc)$_2$(py)$_2$Fe$_2$(μ-C)	911 (IR)	477 (RR)	[31]
[(pc)$_2$Fe$_2$(μ-C)]	990 (IR)	n. r.	[32]
[(tpp)$_2$Fe$_2$(μ-O)]	876 (IR)	363 (RR)	[33]
[(pc)$_2$Fe$_2$(μ-O)]	820, 854 (IR)	n. r.	[20b]

n. r. = not reported; $(tpp)^{2-}$ is the tetraphenylporphinato dianion and $(pc)^{2-}$ the corresponding phthalocyaninato(2 –); py represents pyridine.

We have recorded RR spectra in the range 300 – 700 cm^{-1} of [{L(Cl$_4$-cat)Fe^{IV}}$_2$(μ-N)]Br in acetone at excitation wavelengths of 568, 520, 442, and 407 nm. In this region two prominent bands at 414 and 569 cm^{-1} are observed. The latter displays its highest intensity with 568 and 520 nm excitation and the former is more strongly resonance enhanced at shorter excitation wavelengths (442 and 407 nm). The band at higher energy is therefore assigned to the ν(Fe – O$_{cat}$) stretch, whereas the latter is attributed to the ν_s(Fe-N-Fe) stretch. ν(Fe – O$_{cat}$) has also been observed in the infrared spectrum at 570 cm^{-1}. This mode has also been observed in the IR and RR spectra of **10** at 530 and 544, of **9** at 556 and 558, and of [{L(Cl$_4$-cat)Fe^{IV}}$_2$(μ-N)]Br at 570 and 569 cm^{-1}. Thus with increasing formal oxidation state of the iron ions (and decreasing Fe – O$_{cat}$ bond length) the energy of the (Fe – O$_{cat}$) mode increases. It is noteworthy that we did not observe two ν(Fe – O$_{cat}$) frequencies for **9**, which contains an asymmetric [Fe(μ-N)Fe]$^{4+}$ core with localized valencies.

Electronic and EPR spectra and magnetic properties of complexes: Electronic spectra of complexes in acetonitrile were recorded at room temperature in the range 220 – 1500 nm; the results are summarized in Table 5.

Table 5. Electronic spectra of complexes in acetonitrile solution.

Complex	ν_{max} [nm](ε [L mol^{-1}cm^{-1}])
1	333(1.01×10^4), 370(2.55×10^3), 617(3.9×10^3)
2	333(9.9×10^3), 373(3.7×10^3), 420sh, 606(3.7×10^3)
3	256(3.8×10^3), 333(3.7×10^3), 417(900), 491(600)
4	230(1.9×10^4), 280(2.6×10^4), 365(7.8×10^3)
5	349(2.6×10^4), 475(7.0×10^3)
6	355(2.6×10^4), 415sh, 475sh, 866(300)
7	258(1.22×10^5), 345(3.5×10^4), 555(4.3×10^3), 760sh
8	355(2.2×10^4), 420sh, 470sh, 820(270)
[LFe^{III}(Cl$_4$-cat)Cl][10]	304(7.8×10^3), 460(1.64×10^3), 704(2.4×10^3)
[LFe^{III}(Cl$_4$-cat)(N$_3$)][10]	306(8.6×10^3), 411(3.3×10^3), 680(2.5×10^3)
10[10]	260(1.63×10^4), 304(1.43×10^4), 491(5.0×10^3)
[{L(Cl$_4$-cat)Fe}$_2$(μ-N)][10]	328(1.7×10^4), 423(4.9×10^3), 442sh, 876(300)
9[10]	228(5.5×10^4), 267(8.9×10^4), 316(3.3×10^4), 523(2.2×10^3), 617(1.7×10^3), 770(1.1×10^3)

The electronic spectra are dominated in the visible region by intense charge transfer (CT) bands:

i) Catecholate-to-iron CT are observed in the range 600 – 710 nm in the mononuclear species **1**, **2**, [LFe(Cl$_4$-cat)Cl], and [LFe(Cl$_4$-cat)(N$_3$)]; they are hypsochromically shifted to 470 – 500 nm in the oxo-bridged species **5** and **10**; acetylacetonate-to-iron CT bands are less intense at 490 nm in **3** and 365 nm in **4**.

ii) Oxo-to-iron CT bands of linear [Fe(μ-O)Fe]$^{4+}$ cores are observed in the 300 – 400 nm range; the p_x, p_y(oxo) $\rightarrow d_{xz}, d_{yz}$(Fe^{III}) CT band in **4** is observed at 365 nm.[29] In **5** and [{L(Cl$_4$-cat)Fe^{III}}$_2$(μ-O)] this band is obscured by strong $\pi \rightarrow \pi^*$ transitions of the catecholate ligands.

iii) Complexes **6**, **8**, and **9** that contain the asymmetric [Fe(μ-N)Fe]$^{4+}$ core ($S = 3/2$) display a shoulder at 420 nm which we assign to a CT transition of the [Fe(μ-N)Fe]$^{4+}$ moiety. This assignment is based on the observation that excitation in resonance with this band enhances the ν_{as}(Fe-N-Fe) band at 911 cm^{-1} (see above). The absorption maximum at $\approx$450 nm in these three complexes is due to the catecholate-to-iron CT (excitation into this band at

482 nm enhances the $\nu(Fe-O_{cat})$ stretching mode at 558 cm^{-1}).

iv) All complexes with a $[Fe(\mu\text{-}N)Fe]^{4+}$ core ($S=3/2$) display an intervalence band of intermediate intensity ($\varepsilon \approx 300\ L\,mol^{-1}cm^{-1}$) at 866 nm for **6**, 820 nm for **8**, and 876 nm for **9**. This absorption maximum is absent in the spectra of complexes which contain the symmetric $[Fe(\mu\text{-}N)Fe]^{5+}$ core; for example **7** and $[\{L(Cl_4\text{-cat})\text{-}Fe^{IV}\}_2(\mu\text{-}N)]Br$.

v) The spectra of **7** and $[\{L(Cl_4\text{-cat})Fe^{IV}\}_2(\mu\text{-}N)]Br$ display two or three intense CT bands in the range 500–800 nm which we cannot assign at this point.

X-band EPR spectra of solutions of complexes **6**, **8**, and **9** in acetonitrile or dichloromethane were recorded under non-saturation conditions in the temperature range 5.4–77 K. The spectra were analyzed on the basis of a spin Hamiltonian description of the fine structure of a spin quartet ground state $S_t=3/2$ [Eq. (4)], where D and E/D are the usual zero-field splitting and rhombicity parameters.[35]

$$H_e = D[S_z^2 + \tfrac{1}{3}S(S+1) + E/D(S_x^2 - S_y^2)] + \mu_B \boldsymbol{S}\bar{\bar{g}}_e\boldsymbol{B} \quad (4)$$

Under the influence of the zero-field terms, the spin states splits into two Kramers doublets which in the purely axial case ($E/D=0$) are characterized by the eigenvalues of S_z, as $|\pm 3/2>$ and $|\pm 1/2>$. The zero-field splitting of the doublets is $2D$ and for positive D values the $|\pm 1/2>$ doublet is lowest. For large D ($\gg h\nu = 0.3\ cm^{-1}$ at X-band) EPR transitions occur only within Kramers doublets. In this case the EPR absorption-derivative spectra of frozen solutions or powder samples are characterized by signals at three *effective g* values (g_x, g_y, g_z) which can be theoretically derived from matrix elements of the spin Hamiltonian [Eq. (4)].[35] In axial symmetry ($E/D \approx 0$) only the $|\pm 1/2>$ doublet is EPR-active with $g_x \approx g_y \approx 4$ and $g_z \approx 2$. This situation is encountered in the spectra of **8** as shown in Figure 6; the spectra of **6** and $[\{L(Cl_4\text{-cat})Fe\}_2(\mu\text{-}N)]$ are very similar. The powder simulation for **8** with effective g values and Lorentzian lines is depicted in Figure 6. The results for g_x, g_y and g_z for the three mixed-valence complexes are given in Table 6. The zero-field splitting, $2D$, of the $S_t=3/2$ ground multiplet was derived from the temperature dependence of the EPR intensities (doubly integrated spectra). As only the $|\pm 1/2>$ doublet is EPR-active, the product intensity × temperature, *IT*, is proportional to the Boltzmann population of this resonant doublet as depicted in Equation (5).

$$IT = \text{constant}(1 + e^{-2D/kT}) \quad (5)$$

The experimental data and the corresponding fit for **8** are shown in Figure 6. The rhombicity estimated from first-order perturbation expression from the difference of the effective g values, $g_y - g_x = 12\,E/D$, is less than 0.01 in all cases.

In order to obtain an estimate for the electronic g_e values of the spin $S_t=3/2$ we assume axial symmetry for the $\boldsymbol{g}_e$ tensor. The components of g_e are then given by $g_{e\parallel}=g_z$; $g_{e\perp} = 1/2(g_x+g_y)/(S+1/2)$ as is derived from a comparison of the matrix elements for the $|3/2, \pm 1/2>$ doublet given by the Hamiltonian in Equation (4) and the corresponding fictitious

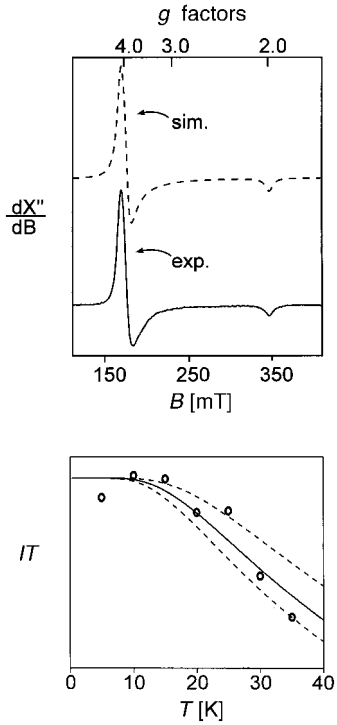

Figure 6. Temperature-dependent X-band EPR spectra of **8** in CH_3CN (top) and a plot of the product intensity · temperature (*IT*) versus temperature (bottom). Experimental conditions: microwave frequency 9.653 GHz, microwave power 20 μW, modulation amplitude 1 mT, modulation frequency 100 kHz. The simulation (top) is performed with effective g values given in Table 7 and Lorentzian line shapes. The solid line in the *IT* versus T plot represents a fit to Equation (4) with $D = 21\ cm^{-1}$ and 14 and 22 cm^{-1} (broken lines).

Table 6. X-Band EPR spectra of mixed-valent complexes containing an $[Fe^{III}(\mu\text{-}N)Fe^{IV}]^{4+}$ core and of mononuclear species.

Complex	g_x[a]	g_y[a]	g_z[a]	D [cm^{-1}][b]	E/D[c]	$g_{e\perp}$[d]
9	3.99	4.14	2.00	13 ± 5	0.013	2.03
6	4.00	4.12	2.00	7 ± 3	0.010	2.03
8	3.96	4.07	1.98	21 ± 5	0.009	2.01
3	5.8	6.3	2.0		0.010	2.02
$[LFe(Cl_4\text{-cat})(N_3)]$	5.7	6.5	2.0		0.017	2.03

[a]Effective g values obtained from spectral simulations. [b] Zero-field splitting parameter taken from temperature dependence of EPR intensities. [c] Rhombicity, calculated from first-order perturbation expressions $\Delta g_{x,y} = 12\ E/D$ for $S=3/2$ and $\Delta g_{x,y} = 48\ E/D$ for $S=5/2$ (valid for $|S, \pm 1/2>$ doublets). [d] Electronic g values calculated from $g_\perp = g_{e\perp}(S+1/2)$, valid for $E/D \approx 0$, where $g_\perp = (g_x + g_y)/2$, note $g_{e\parallel} = g_z$ for $|S, \pm 1/2>$ doublets.[35]

Hamiltonian with effective spin $S^{eff}=1/2$.[35] Under the assumption of i) fully localized valencies, ii) antiferromagnetic coupling between $S_1=5/2$ for Fe^{III} and $S_2=1$ for Fe^{IV}, and iii) $g^{Fe^{III}}=2$, spin projection techniques yield for the $Fe^{III}Fe^{IV}$ dimer the local g_e values for Fe^{IV} according to Equation (6).

$$g_e(S=3/2) = -2/5\,g^{Fe^{IV}} + 7/5\,g^{Fe^{III}} \quad (6)$$

This procedure yields the values $g^{Fe^{IV}} =$ 1.93, 1.93, and 2.0 for both **6** and **9** and the values 1.98, 1.98, and 2.05 for **8**. These values are too small if one considers calculated local Fe^{IV} g values of about 2.2, 2.2, and 1.99 from $D = 20\ cm^{-1}$ and a spin-orbit coupling constant of $\xi \approx 350\ cm^{-1}$ for an Fe^{IV} ion.[36] In

0947-6539/99/0502-0800 $ 17.50+.50/0 *Chem. Eur. J.* **1999**, *5*, No. 2

particular the low $g_{e\perp}$ values are not consistent with the existence of a localized $Fe^{IV}(3d^4)$ low-spin configuration. This result, together with those of the MO calculations (vide infra), is an indication that the description of complexes which contain an asymmetric $[Fe(\mu\text{-}N)Fe]^{4+}$ core by means of localized, pure Fe^{III} and Fe^{IV} oxidation states is not quite appropriate and strong covalent bonding in this unit prevails. We note, however, that hyperfine coupling of electron spin density with the nuclear spin of ^{14}N could not be detected in the EPR spectra, not even at lower microwave frequencies (S-band, data not shown). Non-resolved hyperfine splittings must be overall smaller than the experimental linewidth of 2.2 mT at $g = 4$. This indicates that the spin density at the bridging nitrogen cannot be as high as it might be in the valence-delocalized complex $[(tpp)Fe^{3.5}(\mu\text{-}N)Fe^{3.5}(pc)]$ for which the appearence of ^{14}N hyperfine splitting has been noted.[14a]

The X-band EPR spectra of solutions of the mononuclear species **3** and $[L(Cl_4\text{-cat})Fe(N_3)]$ in acetonitrile at 4 K display a nearly axial signal at effective $g_{x,y} \approx 6$ and $g_z \approx 2$, $E/D \approx 0.01$. These spectra are typical for octahedral high-spin Fe^{III} systems ($S = 5/2$). In agreement with this, the mononuclear species **1**, **2**, and **3** display temperature-independent magnetic moments of 5.76 μ_B, 5.72 μ_B, and 5.91 μ_B (40–295 K), respectively. This is close to the spin-only value of 5.93 μ_B expected for a high-spin Fe^{III} ($S = 5/2$) ion.

In contrast, the magnetic moments of the (μ-oxo)diferric complexes **4**, **5**, **10**, and $[\{L(Ph_2acac)Fe^{III}\}_2(\mu\text{-}O)](BPh_4)_2$ as well as $[\{(tacn)(acac)Fe^{III}\}_2(\mu\text{-}O)](ClO_4)_2$ (tacn = 1,4,7-triazacyclononane) were found to decrease strongly with decreasing temperature yielding a diamagnetic $S = 0$ ground state.[37] The data were fitted by means of least-squares methods to the theoretical expression for the molar magnetic susceptibility, χ_M, with the usual spin Hamiltonian $H = -2J S_1S_2$ with local spins $S_1 = S_2 = 5/2$. A mononuclear paramagnetic impurity ($S = 5/2$) was included in order to fit the low-temperature data appropriately. The g value was fixed at 2.0. The results are given in Table 7.

For complexes **6**, **8**, and $[\{L(Cl_4\text{-cat})Fe\}_2(\mu\text{-}N)]$ with an $[Fe(\mu\text{-}N)Fe]^{4+}$ core, the magnetic moment per dinuclear unit is temperature-independent in the range 30–295 K at 3.9 μ_B which corresponds to the spin-only value for an $S = 3/2$ ground state, the only populated state up to room temperature. Below 30 K, the magnetic moment decreases with decreasing temperature due to zero-field splitting. From a simulation $|D| = 10 \pm 5$ cm^{-1} was found with $g = 2.0$ (fixed) in reasonable agreement with the EPR measurements of the three complexes in solution. Figure 7 shows the temperature-dependence of the magnetic moment of **8**. The samples were contaminated with $\approx 10\%$ of the corresponding (μ-oxo)diferric analogue (as judged from the Mössbauer spectra). Since their magnetism is known we have subtracted their contributions from the susceptibility data of the (μ-nitrido)diiron complexes. These measurements indicate that a very strong intramolecular antiferromagnetic coupling with $|J| > 250$ cm^{-1} between a high-spin Fe^{III} ($S = 5/2$) and a low-spin Fe^{IV} ($S = 1$) ion prevails in complexes with an asymmetric $[Fe(\mu\text{-}N)Fe]^{4+}$ core in accordance with the MO calculations (vide infra).

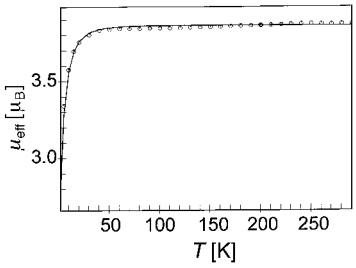

Figure 7. Plot of the effective magnetic moment of **8** versus the temperature. The solid line represents a fit of the data from Equation (4) with $D = 10$ cm^{-1} and $g = 2.0$. The experimental values are corrected for diamagnetic contributions of 530×10^{-6} cm^3 mol^{-1}. The simulations were consistent with up to 6% contamination with (μ-oxo)diferric compound (antiferromagnetically coupled $J \approx 100$ cm^{-1}). Because of increased ambiguity, this contribution was not considered here.

Complexes **7** and $[\{L(Cl_4\text{-cat})Fe^{IV}\}_2(\mu\text{-}N)]PF_6$ are diamagnetic even at room temperature. Strong intramolecular antiferromagnetic coupling between two low-spin Fe^{IV} ions leads to the observed $S = 0$ ground state with a lower limit of $|J| = 250$ cm^{-1}.

Mössbauer spectra: Mössbauer spectra of polycrystalline samples were recorded in the temperature range 4.2–200 K and with applied fields of 0–7 T. The results are given in Tables 8 and 9.

The zero-field Mössbauer spectra of mononuclear **3** and $[L(Cl_4\text{-cat})Fe(N_3)]$ each consist of a quadrupole doublet with isomer shift and quadrupole splitting parameters typical for octahedral high-spin ferric ions. In contrast, the spectrum of $[LFe^{II}(Ph_2acac)]BPh_4$ shows a doublet with a much larger isomer shift, $\delta = 1.10$ mm s^{-1}, and a considerably larger quadrupole splitting of 2.61 mm s^{-1} at 80 K. The high-spin complexes $[L(Cl_4\text{-cat})Fe^{II}NCCH_3]\cdot 2H_2O$ and $[L(Ph_2acac)Fe^{II}Cl]$

Table 7. Comparison of structural data and exchange coupling constants of (μ-oxo)diferric complexes.

Complex	av. Fe–O_b, [Å]	Fe-O-Fe, [°]	J, [cm^{-1}] [a]	J_{calcd} [cm^{-1}][b]	PI[c]	Ref.
$[\{(tacn)(acac)Fe\}_2O](ClO_4)_2$	1.787(5)	158.6(3)	–122	–130(–102)	0.01	[27]
4	1.806(2)	180	–100	–102(–86)	0.04	this work
5	1.799(1)	180	–90	–112(–91)	1.63	this work
$[\{L(Ph_2acac)Fe\}_2O](ClO_4)_2$	1.811(1)	180	–95	–96(–82)	2.6	[23]
10	1.804(1)	180	–95	–105(–87)	1.85	[10]
$[\{LFe\}_2(\mu\text{-}O)(\mu\text{-}ac)](PF_6)_2$	1.800(3)	119.7(1)	–119	–111(–112)		[38]
$[L(Ph_2acac)Fe(\mu\text{-}O)Fe(Cl_4\text{-cat})L]ClO_4$	1.806	173.7(2)	–90	–102(–86)		[23]

[a] Experimental coupling constant; $H = -2JS_1S_2$ ($S_1 = S_2 = 5/2$) $g = 2.0$ (fixed). [b] Calculated coupling constant according to the expression given by Gorun and Lippard[39] and in parenthesis that of Weihe and Güdel.[40] [c] Paramagnetic impurity with $S = 5/2$, given in molar percentage.

Table 8. Zero-field Mössbauer parameters of complexes.[a]

Complex	T [K]	Fe site	δ [mm s^{-1}][b]	ΔE_Q [mm s^{-1}][c]	Γ [mm s^{-1}][d]	relative intensities, %	Ref.
3	80		0.45	0.86	0.65	100	this work
[LFe(Cl$_4$-cat)(N$_3$)]	3.7		0.43	0.98	0.40	100	[10]
[LFe^{II}(Ph$_2$acac)](BPh$_4$)	80		1.10	2.61	0.32	100	this work
4	80		0.44	1.27	0.38	100	this work
5	80		0.44	1.44	0.30	100	this work
10	77		0.40	1.38	0.29	100	[10]
6	80	Fe^{III}	0.44	1.45	0.70	40	this work
		Fe^{IV}	0.07	0.85	0.38	41	
		Fe-O-Fe	0.45	1.44	0.18	19	
9	77	Fe^{III}	0.52	1.67	0.77	45	this work, [10]
		Fe^{IV}	0.09	0.81	0.22	45	
		Fe-O-Fe	0.48	1.41	0.26	10	
7	4.2		0.03	1.62	0.26	100	this work
8 · BPh$_4$	80	Fe^{III}	0.60	2.00	1.70	44	this work
		FeIV	0.04	1.13	0.31	44	
		Fe-O-Fe	0.46	1.51	0.34	12	
[{LFe(Cl$_4$-cat)}$_2$(μ-N)]Br	77		0.04	1.55	0.26	100	this work, [10]
[(tpp)$_2$Fe$_2$(μ-N)]ClO$_4$	131		0.03	2.00	n. r.	100	[41]
[(pc)$_2$Fe$_2$(μ-N)]PF$_6$	77		−0.10	2.06	0.16	100	[15d]
[(tpp)$_2$Fe$_2$(μ-N)]	131		0.18	1.08	n. r.	100	[41]
[(pc)$_2$Fe$_2$(μ-N)]	77		0.06	1.76	0.19	100	[15d]

[a] Ligand abbreviations see Scheme 1 and tpp. represents the tetraphenylporphinate(2 –) and pc is the phthalocyaninate(2-) ligand. [b] Isomer shift. [c] Quadrupole splitting. [d] Full width at half maximum.

Table 9. Mössbauer hyperfine parameters of [Fe(μ-N)Fe]$^{4+}$ complexes at 4.2 K.

Complex	Site	δ[a] [mm s^{-1}]	ΔE_Q[b] [mm s^{-1}]	η[c]	$A/(g_N\mu_N)$, T[d]	Rel. int. [%][e]
8	Fe^{IV}	0.05	+1.10	0.2	6.0, 6.0, 1.6 (4.5)[f]	45
	Fe^{III}	0.60	−2.05	0.4	−23.0, −23.0, −9.0 (−18.3)[f]	45
6	Fe^{IV}	0.10	+0.77	0.8	+5.2	40
	Fe^{III}	0.49	−1.51	0.5	−22.0	40
9	Fe^{IV}	0.10	+0.77	0.8	+5.5	40
	Fe^{III}	0.46	−1.60	0.5	−22.0	40

[a] Isomer shift. [b] Quadrupole splitting. [c] Asymmetry parameter. [d] Hyperfine tensor, for **6** and **9** only isotropic values could be determined. [e] The sample contained ≈10% (**8**), ≈20% (**6**) of the corresponding (μ-oxo)diferric species. [f] Isotropic contribution ⅓ Tr $A/(g_N\mu_N)$.

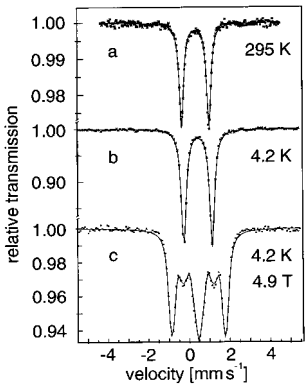

Figure 8. Mössbauer spectra of **10** at 295 and 4.2 K in a zero magnetic field and at 4.2 K with a field of 4.9 T parallel to the λ-beam.

exhibit a quadrupole doublet at 80 K with $\delta = 1.06$ mm s^{-1}, $\Delta E_Q = 1.54$ mm s^{-1}, and $\delta = 1.11$ mm s^{-1}, $\Delta E_Q = 2.52$ mm s^{-1}, respectively. These parameters are all compatible with five-fold or sixfold coordination of high-spin Fe^{II} in these complexes.

The zero-field Mössbauer spectra of the (μ-oxo)diferric complexes **4**, **5**, and [{L(Cl$_4$-cat)Fe^{III}}$_2$(μ-O)] also consist of a single quadrupole doublet where both the isomer shift and quadrupole splitting are temperature-dependent. Figure 8 shows the typical spectra of **10** at 4.2 and 295 K. In general, the isomer shift varies due to second-order Doppler shift in the range 0.46 – 0.33 mm s^{-1} at temperatures 4.2 to 350 K and the quadrupole splitting varies from 1.35 to 1.41 mm s^{-1} (1.44 – 1.39 mm s^{-1} for **5**). The spectra in an applied field of 4.9 T at 4.2 K (Figure 8) display the pattern of mixed nuclear quadrupole and Zeeman interactions for a diamagnetic ground state. From simulations which use only the usual nuclear Hamiltonian[42] with applied field (without internal field, $S = 0$) the asymmetry parameter η was determined to be in the range 0.8 – 1.0, which indictaes a strong non-axial distortion of the iron site. These data are in accord with many other reports on (μ-oxo)diferric complexes.[2a, 37]

The Mössbauer spectra of the complexes **7** and [{L(Cl$_4$-cat)Fe^{IV}}$_2$(μ-N)]Br which contain the symmetric [Fe^{IV}(μ-N)-Fe^{IV}]$^{5+}$ core with an $S = 0$ ground state are similar to those of the (μ-oxo)diferric species; they display a single quadrupole doublet albeit at a much smaller isomer shift in accord with the high oxidation state of iron ($\delta = 0.03$ and 0.04 mm s^{-1} at 4.2 and 77 K, respectively). The zero-field spectrum at 77 K and the spectrum recorded at 4.2 K with applied field of 6.26 T of [{L(Cl$_4$-cat)Fe^{IV}}$_2$(μ-N)]Br are shown in Figure 9. The asymmetry parameter η of 0.5 is smaller than in the oxo-bridged complexes. The quadrupole coupling has a positive sign, $\Delta E_Q = +1.55$ mm s^{-1}, which is typical of a formal low-spin $3d_{xy}{}^2 d_{xz,yz}{}^2$ configuration.

The spectra recorded for complexes **6**, **8**, and **9** containing the mixed-valent [Fe(μ-N)Fe]$^{4+}$ core are qualitatively similar to each other, hence, only that of **8** is shown (Figure 10). The zero-field spectrum consists of three quadrupole doublets in the ratio 44:44:12. At 4.2 K the two subspectra with 44% relative absorption area show the isomer shift of a high-spin

0947-6539/99/0502-0802 $ 17.50+.50/0 Chem. Eur. J. 1999, 5, No. 2

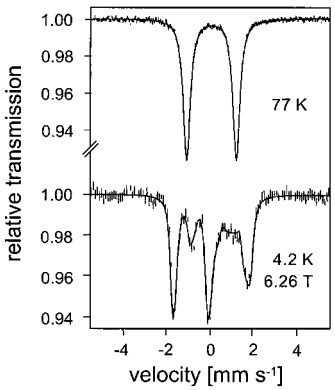

Figure 9. Mössbauer spectra of $[\{L(Cl_4\text{-cat})Fe^{IV}\}_2(\mu\text{-N})]Br$ at 77 K in a zero magnetic field and at 4.2 K with a field of 6.26 T parallel to the γ-beam.

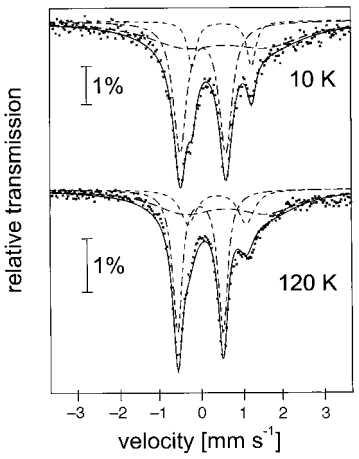

Figure 10. Temperature-dependent, zero-field Mössbauer spectra of **8**.

Fe^{III} ion (0.60 mm s^{-1}) and of a low-spin Fe^{IV} ion (0.05 mm s^{-1}), respectively. The third subspectrum (12%) resembles the spectra of **4**, **5**, and **10** and is therefore assigned to a contamination by a (μ-oxo)diiron species. The linewidth of the doublet of the ferric site is unusually broad which may be due to spin relaxation effects. Clearly, on the Mössbauer time scale (10^{-7} s) the valencies of the two sites in both **6** and **8** are different. We note that the quadrupole splitting of the Fe^{III} ion in the complexes with (μ-N) bridges exceeds the values for Fe^{III} with (μ-O) ligands. This indicates again partial delocalization of the excess electron within the $[Fe(\mu\text{-N})Fe]^{4+}$ unit.

Figure 11 shows the spectrum of **8** in an applied field of 7.0 T at 4.2 K. The spectrum has been simulated for $S = 9/2$ [Eq. (4)] and the usual nuclear Hamiltonian for ^{57}Fe.[42] We again adopted two subspectra for $[Fe(\mu\text{-N})Fe]^{4+}$ ($S = 9/2$) and an additional subspectrum for the μ-oxo contamination ($S = 0$). Isomer shifts, quadrupole splittings and relative intensities were taken from the corresponding zero-field spectra. Electronic $\mathbf{g}_e$ values, D and E/D for the $S = 9/2$ species were taken from the EPR results given in Table 6. (The Mössbauer spectra are consistent with any $D \geq 18$ cm^{-1}.) The hyperfine tensors $\boldsymbol{A}_i$, asymmetry parameters η_i and the sign of the electric field gradient (efg) main component $V_{zz,i}$ for the sites $i = Fe^{III}, Fe^{IV}$ were optimized for three experimental data sets simultaneously, which were measured at 4.2 K, 7 T($\perp\gamma$) (Figure 11); 4.2 K, 3.5 T($\perp\gamma$); 120 K, 7 T($\perp\gamma$) (not shown).

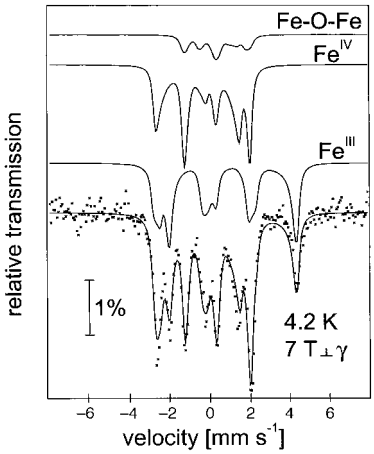

Figure 11. Mössbauer spectrum of **8** at 4.2 K with a field of 7.0 T parallel to the γ-beam. Simulations of sites Fe^{III}, Fe^{IV}, and Fe-O-Fe and the superposition of the three subspectra are shown as solid lines. For the simulation parameters see the text. The parameters for Fe-O-Fe were $\delta = 0.52$ mm s^{-1}, $\Delta E_Q = 1.41$ mm s^{-1}, $\eta = 0.6$, and $\Gamma = 0.3$ mm s^{-1}.

The results are summarized in Table 9. The data of **6** and **9** were successfully analyzed with isotropic $\boldsymbol{A}$ tensors, whereas **8** required anisotropic (axial) tensors. The spectra of all compounds were simulated with the assumption of slow spin relaxation at 4.2 K and fast relaxation at higher temperatures.

Assuming fully localized valencies and antiferromagnetic coupling between $S_1 = 5/2$ and $S_2 = 1$, the effective hyperfine coupling constants, A_i, which are given with respect to total spin $S_t = 3/2$, can be used to calculate local hyperfine constants a_i for the individual Fe^{III} and Fe^{IV} sites as in Equations (7) and (8).

$$a_{Fe^{III}} = 5/7\ A_{Fe^{III}} \quad (7)$$

$$a_{Fe^{IV}} = -5/2\ A_{Fe^{IV}} \quad (8)$$

This procedure yields the following values for **8**: $a_{Fe^{IV}}/(g_N\mu_N)$ between -11.3 and -13.8 T and $a_{Fe^{III}}/(g_N\mu_N)$ between -12.9 and -15.7 T (isotropic contributions), whereas octahedral ferric iron usually has hyperfine constants $a_{Fe^{III}}/(g_N\mu_N)$ of about -22 T.[42] This deviation again indicates partial delocalization of the excess electron within the $[Fe(\mu\text{-N})Fe]^{4+}$ unit as discussed below. The spectra of **6** and **9** were analyzed analogously (Table 9). Even though the simulated results are qualitatively similar to those of **8**, a comparison of the Mössbauer data in Table 9 reveals some distinct differences between the parameters of the two *symmetrically* coordinated species **6** and **9** and the *asymmetrically* coordinated complex **8**. For the latter, the isomer shift of the ferric site is larger (i.e. more Fe^{III}-like), while that of the ferryl site is smaller (more Fe^{IV}-like) than the corresponding values of the two other species. We take this as an indication that the valencies in **8** are more localized than in their symmetric counterparts.

Molecular orbital calculations: The smallest system among the asymmetrically nitrido-bridged mixed-valence dimers is complex **9** which has been chosen as a representative example for the calculations. Even this complex contains 93 atoms and

Table 10. Orbital energies ε_i and composition (in %) of the spin-up (left) and spin-down (right) orbitals with more than 20% Fe(3d) participation for **9**. The HOMOs are marked by an asterisk.

ε_i[eV]	Fe^{III}(3d)	Fe^{IV}(3d)	N_μ(2p)	ε_i[eV]	Fe^{III}(3d)	Fe^{IV}(3d)	N_μ(2p)
– 3.22	5	42(xz)	42	– 2.03	70(x^2-y^2)	0	0
– 3.24	5	40(yz)	46	– 2.34	73(z^2)	1	4
– 3.58	2	62(z^2)	5	– 3.11	50(xz)	16	27
– 3.84	1	64(x^2-y^2)	4	– 3.14	50(yz)	17	26
– 4.30*	48(x^2-y^2)	1	1	– 4.03	4	61(z^2)	2
– 4.91	52(z^2)	3	4	– 4.06	94(xy)	3	0
– 5.90	0	97(xy)	0	– 4.08	6	60(x^2-y^2)	1
– 6.32	30(yz)	6	0	– 4.65*	35(xz)	35(xz)	19
– 6.39	33(xz)	7	0	– 4.71	30(yz)	40(yz)	19
– 7.01	8	26(yz)	13	– 6.35	0	97(xy)	0
– 7.03	9	26(xz)	13	–			
– 7.30	93(xy)	0	0	–			
– 7.88	23(yz)	0	3	–			
– 7.94	29(xz)	0	2	–			
– 8.10	27(xz/yz)	0	0	– 8.72	0	22(xz/yz)	8
– 8.61	10(xz/yz)	18(xz/yz)	11	– 8.95	1	32(yz)	26
– 8.73	19(xz/yz)	22(xz/yz)	20	– 9.01	2	19(xz)	20

256 valence orbitals so that the calculations become rather time consuming. However, a first series of test calculations showed that the methyl groups in L may be substituted by hydrogen atoms without changing the electronic structure at the iron centers. The same is true if all chlorine atoms of the tetrachloro-catecholate are replaced by hydrogen atoms provided that they are artificially modified in a way that they carry the same effective charge as the chlorines. This system contains 75 atoms and 196 valence orbitals and requires 228 seconds CPU time per iteration on a VAX6000/610 computer. The next series of MO calculations based on the experimental geometry revealed that the theoretical results are neither in accordance with the measured Mössbauer data nor with the expected spins of ½ and 1, respectively, at the two iron centers. Attributing these failures to the low accuracy of the μ-N position,[10] this position has been optimized to yield a flat minimum in the total energy for an Fe^{IV}–N_μ distance of 1.59 Å compared with the experimental value of 1.50(8) Å. Therefore, this theoretically determined value has been used in the subsequent calculations for **9**.

The rather complicated pattern of the Fe(3d) orbital energies may be easier understood by comparison with a typical high-spin Fe^{III} center in a weak octahedral ligand field. In such a case, the energy spectrum is dominated by the exchange splitting of about 4 eV between the spin-up and the spin-down 3d orbitals of iron. The stabilization of the majority spin (spin-up) orbitals usually leads to strong covalent interactions with the ligand MOs, whereas the destabilized, unoccupied minority spin (spin-down) orbitals are well above the highest occupied MO (HOMO). Due to the differences in σ- and π-type metal–ligand orbital interactions, both sets of orbitals will be split into the triply degenerate π-type t_{2g} and into the doubly degenerate σ-type e_g manifold. The ordering of the minority spin orbitals follows the expectations from ligand-field theory, while the majority spin orbitals very often exhibit an inverted bonding scheme as a consequence of the colvalent interactions.[43]

Several of these general features can be identified in the orbital energy pattern of **9** (cf Table 10). Among the occupied spin-up orbitals, the two highest are the $Fe^{III}(e_g)$-type orbitals, another two MOs are almost pure $3d_{xy}$ orbitals of Fe^{III} and Fe^{IV}, whereas the $Fe^{III}(3d_{xz,yz})$ orbitals contribute to seven MOs. Additionally, four MOs contain appreciable admixtures from the $Fe^{IV}(3d_{xz,yz})$ orbitals. The four lowest unoccupied MOs are mainly Fe^{IV}(3d)-orbitals, two of them exhibiting considerable participation from the bridging nitrogen. In an idealized notation, this results for the spin-up orbitals in the electronic configuration $Fe^{III}(3d^5_\uparrow)Fe^{IV}(3d^1_\uparrow)$ for the iron centers in **9**.

Among the spin-down MOs the lowest seven unoccupied orbitals are easily identified as Fe(3d) orbitals, five of which belong to Fe^{III} and the remaining two to Fe^{IV}. However, only one of the occupied orbitals exhibits more than 50% contribution from an atomic orbital of one iron, namely $Fe^{IV}(3d_{xy})$. The two highest occupied MOs have mainly $3d_{xz,yz}$ character, but they cannot be unambigously assigned to one of the two iron atoms because both contribute approximately with the same amount. This is in line with the relatively low $Fe^{III}(3d_{xz,yz})$ participation of 50% in the corresponding unoccupied MOs. Finally, two MOs at an energy around 9 eV show strong N_μ-Fe^{IV} π-bonding character. Altogether this indicates the existence of considerable (dpdπ) charge and spin delocalization over the whole $Fe^{III}(\mu$-N)Fe^{IV} unit.

Since this delocalized π interaction (mostly within the spin-down orbitals) essentially determines the electronic properties of the nitrido-bridged complexes, it will be described in more detail (Figure 12). Starting from the three atomic orbitals $2p_y(N_\mu)$, $3d_{yz}(Fe^{III})$ and $3d_{yz}(Fe^{IV})$, three linear combinations can be formed. The strongest interaction takes place between N_μ and Fe^{IV}, and leads to a bonding and to an antibonding MO separated by about 5 eV. The $3d_{yz}$ orbital of Fe^{III} does not contribute significantly to the bonding combination, whereas the interactions between the antibonding combination and the $3d_{yz}(Fe^{III})$ orbital gives a splitting of 1.57 eV into a bonding and antibonding combination with respect to Fe^{III}–N_μ. Analogous conclusions hold for the x-type orbitals. Due to this pronounced (dp dπ) interaction, the d-orbital splitting pattern of both iron sites does not resemble that of a distorted octahedron, even in case of Fe^{III}. For the splitting within the t_{2g} type orbitals $Fe^{III}(3d_{xy\downarrow})$ and

0947-6539/99/0502-0804 $ 17.50+.50/0 *Chem. Eur. J.* **1999**, *5*, No. 2

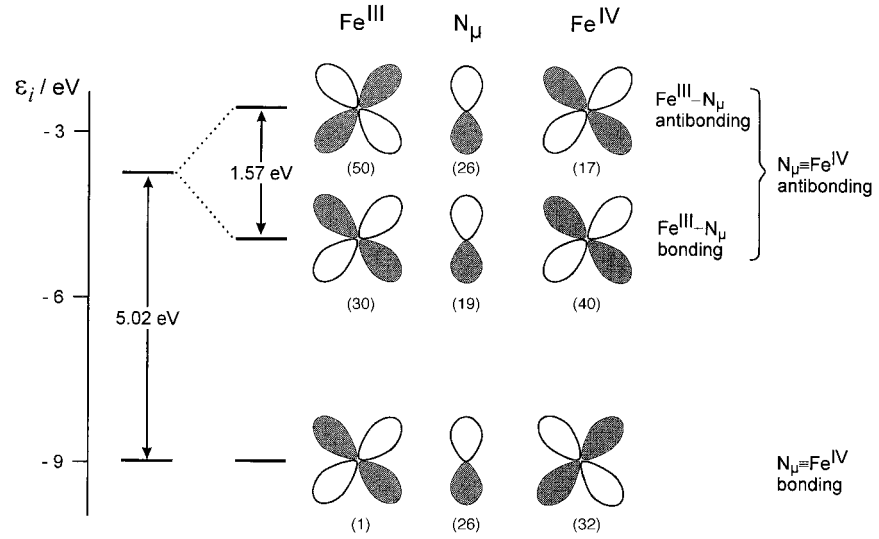

Figure 12. Schematic representation of the different (dpdπ) interactions among the spin-down orbitals in **9**. Numbers in brackets denote the percentage contribution of the respective atomic orbital.

$Fe^{III}(3d_{xz,yz\downarrow})$ is larger (0.92 eV) than the 0.77 eV between $Fe^{III}(3d_{xz,yz\downarrow})$ and the e_g type $Fe^{III}(3d_{z^2\downarrow})$ orbital (cf. Table 10). The minority-spin orbitals of Fe^{IV} exhibit still larger deviations since the $e_{g\uparrow}$ type orbitals lie between $Fe^{IV}(3d_{xy\uparrow})$ and $Fe^{IV}(3d_{xz,yz\uparrow})$ that are now the highest lying 3d orbitals due to the (dp dπ) interaction.

The strong (dp dπ) delocalization also affects the charge and spin density distribution. The data characterizing the electronic environment of iron, namely effective charges Q(A) and overlap populations n(AB) of next neighbors, show (Table 11) that the overlap populations of Fe^{III} (**10**) with its

Table 11. Charge and spin-density distribution around the iron sites in **9** and **10**.

	Q(Fe)	$n(FeX_\mu)$	$n(FeN_{eq})$	$n(FeN_{ax})$	$n(FeO_{cat})$	n_{3d}	σ_{3d}[a]
Fe^{III}(**10**)	0.86	0.42	0.14	0.08	0.21	6.09	+3.74
Fe^{III}(**9**)	0.71	0.48	0.16	0.08	0.22	6.19	+3.48
Fe^{IV}(**9**)	0.72	0.89	0.21	0.11	0.26	6.18	-0.53

[a] Spin density in units of e.

neighbours are slightly smaller compared with Fe^{III} (**9**), and both are distinctly smaller than those for Fe^{IV} (**9**). These results confirm, as expected, that the bonding of the iron atoms in the oxo-bridged complex is more ionic in character than in the nitrido-bridged complex. Moreover, comparison of Fe^{III} (**9**) and Fe^{IV} (**9**) emphasizes that metal–ligand bonding becomes more covalent in character with increasing oxidation state of the metal atom. This is in accordance with the observation that, under otherwise equal conditions, the ligand-field splitting 10 Dq is larger for higher oxidation states. Finally, due to the strong (dp dπ) interaction, the two highest occupied spin-down MOs cannot be unambigously assigned to one of the two iron atoms because both contribute approximately the same amount. Consequently, the concept of an oxidation state becomes ill-defined in **9** unless Fe^{IV} and N_μ are considered as a unit so that the two highest occupied orbitals can be assigned to this part of the complex. This is also in line with an appreciable delocalization of the spin density of 1.01 electrons within the N_μ–Fe^{IV} moiety where 0.53 electrons are assigned to Fe^{IV} and 0.48 electrons to N_μ. However, LDA methods usually overemphasize delocalization so that a somewhat higher spin density than 0.53 at Fe^{IV} (**9**) seems to be likely. The relatively large spin density of 0.48 p electrons at N_μ is still in accordance with the EPR spectra (s density is found to be negligibly small: 0.0024 electron). Based on a coupling constant $A/g_N\mu_N = 3.4$ mT at $g = 2$ for one p electron[44] one expects an overall ^{14}N ($I = 1$) splitting of 1.6 mT at $g = 4$, which cannot be resolved within the experimental linewidth.

Turning next to the calculated Mössbauer data, the quadrupole splitting ΔE_Q for the oxo-bridged complex **10** is obtained as -1.26 mm s^{-1}. The direction V_{zz} of the efg deviates by 17° from the Fe–Fe axis and points approximately between the two catecholate oxygens. In the principal axes system of the efg tensor, the efg can be decomposed with respect to a basis of atomic orbitals into three parts, denoted as valence, covalence, and ligand contribution,[55] and ΔE_Q correlates directly with the sum of these three contributions. Among these, usually the valence part is dominating which is roughly proportional to the anisotropy $\Delta n_d = n_{x^2-y^2} + n_{xy} - n_{z^2} - (n_{xz}+n_{yz})/2$ of the Fe(3d) shell occupation. For ΔE_Q (**10**) the valence contribution is obtained as -0.73 mm s^{-1}, while the covalence and ligand contributions amount to -0.25 mm s^{-1} and -0.27 mm s^{-1}, respectively. Furthermore, the Fe^{III}(3d) shell occupation $d_\uparrow^{4.94}\ d_{xy\downarrow}^{0.12}\ d_{xz\downarrow}^{0.24}\ d_{yz\downarrow}^{0.23}\ d_{z2}^{0.26}\ d_{x2-y2\downarrow}^{0.22}$ shows that the quadrupole splitting arises exclusively from the covalent interactions of the Fe($3d_\downarrow$) orbitals with the ligand orbitals. Finally, the main reason for the relatively large negative quadrupole splitting is a reduced population of the noninteracting Fe($3d_{xy\downarrow}$) orbital so that there is no compensation for the Fe($3d_{xz,yz\downarrow}$) occupation.

The corresponding analysis for the nitrido-bridged complex **9** yields qualitatively similar results for Fe^{III}. The calculated ΔE_Q value is -1.65 mm s^{-1}, and is thus in close agreement with experiment. The major contribution is the valence part with -1.28 mm s^{-1}, while the covalence and ligand contribution are -0.15 mm s^{-1} and -0.22 mm s^{-1}, respectively. The calculated asymmetry parameter $\eta = 0.40$, and the angle of the efg with the Fe–Fe axis is 7°, also pointing in the direction of the bisector of the O_{cat}-Fe^{III}-O_{cat} angle. The Fe^{III}(3d) shell occupation $d_\uparrow^{4.83}\ d_{xy\downarrow}^{0.02}\ d_{xz\downarrow}^{0.46}\ d_{yz\downarrow}^{0.45}\ d_{z2}^{0.21}\ d_{x2-y2\downarrow}^{0.22}$ in **9** with an increase of the $d_{xz,yz\downarrow}$ population by a factor of two when compared with the oxo-bridged complex **10**, emphasizes the significance of the above-mentioned (dp dπ) delocalization. The more negative quadrupole splitting of Fe^{III} in **9** can thus be attributed to

this increased $d_{xz,yz\downarrow}$ population. Finally, due to the strong covalent metal–ligand interactions, the total $3d_{\downarrow}$ occupation of 1.35 electrons for Fe^{III} in **9** is distinctly larger than for Fe^{III} in **10**, and is far away from zero as assumed in ligand-field theory, and reduces the spin-density in the $Fe^{III}(3d)$ shell to 3.48 electrons.

The origin of the small and positive quadrupole splitting of Fe^{IV} is more difficult to understand. The direction of V_{zz} is canted against the Fe–Fe axis by 37° with direction towards the bisector of the O_{cat}-Fe^{IV}-O_{cat} angle. The three contributions to ΔE_Q are obtained as $+1.87\,mm\,s^{-1}$ (valence), $-0.47\,mm\,s^{-1}$ (covalence) and $-0.36\,mm\,s^{-1}$ (ligand). Hence, the valence contribution again dominates but unlike for Fe^{III} the other two contributions have opposite sign. In addition, the anisotropies $\Delta n_{d\uparrow}$ and $\Delta n_{d\downarrow}$ are 0.18 and 0.22, respectively, so that spin-up and spin-down electrons both contribute approximately the same amount to the quadrupole splitting. Finally, the 3d shell population of $d_{\uparrow^{2.83}}d_{\downarrow^{3.35}}$ for Fe^{IV} is far away from the formal $d_{\uparrow^4}d_{\downarrow^3}$ occupation of an assumed Fe^{IV} ion, and confirms that covalent metal–ligand interactions gain importance with increasing oxidation state of the metal.

Significant differences between **10** and **9** exist also with regard to the magnetic properties expressed by the strength of the exchange coupling constant *J*. Whereas the experimentally derived coupling constant is $-95\,cm^{-1}$ for **10**, only a lower bound of $250\,cm^{-1}$ for $|J|$ could be given for **9**. The numerical calculation of *J* within the broken-symmetry formalism[58] reproduces these differences as well. The theoretical coupling constant *J* in **10** equals $-114\,cm^{-1}$, whereas the calculated value of $-947\,cm^{-1}$ for **9** is almost an order of magnitude larger. This large value can be confirmed and understood by utilizing an analytical approximation for the coupling constant[45] that enables an estimation of the ratio between the two coupling constants in **10** and **9**. For linearly bridged dimeric complexes where direct metal–metal interactions are negligible, *J* is roughly proportional to the square of the product of the metal–ligand overlap matrices [Eq. (9)],

$$J \propto \sum_{d,d'} \left(\sum_i S_{di}^{A\mu} S_{id'}^{\mu B} \right)^2 \qquad (9)$$

in which, for example $S_{di}^{A\mu}$ is the overlap matrix between a d-orbital at site A and a valence orbital *i* of the bridging ligand μ. The overlap matrix can be expressed in closed form by a sum of Hankel functions,[46] that is a polynomial $k_l(x)$ times e^{-x} with $x \approx (\zeta_d^A + \zeta_i^\mu) R_{A\mu}$ where ζ and $R_{A\mu}$ denote an orbital exponent and the distance between both centers, respectively. Taking the orbital exponents ζ_d^{Fe}, ζ_i^0, ζ_i^N, and the other required data from the converged MO calculations, the ratio $J(\mathbf{9})/J(\mathbf{10})$ is obtained as 5.6. On the basis of the experimental value of $J(\mathbf{10})$ $(-95\,cm^{-1})$ the coupling constant of **9** can thus be estimated as $-532\,cm^{-1}$. Hence, the large value of $J(\mathbf{9})$ originates mainly from the shorter distance between N_μ and Fe^{IV} and the more diffuse valence orbitals of nitrogen compared with oxygen, that is $\zeta_i^N < \zeta_i^O$.

In summary, the MO calculations yield an improved understanding of the bonding modes and intramolecular interactions. The electronic structure around the iron centers is well described, as indicated by the agreement between measured and calculated hyperfine parameters, even though the degree of delocalization and the strength of the covalent interactions within the $[Fe(\mu\text{-}N)Fe]^{4+}$ moiety are slightly exaggerated, as is usually the case within the local density approximation.

Discussion

High-valent (μ-nitrido)diiron complexes containing the low-spin $[Fe^{3.5}(\mu\text{-}N)Fe^{3.5}]^{4+}$ core ($S_t = ½$) were discovered in 1976 by Summerville and Cohen[11] by thermolysis and/or photolysis reactions of azidoiron(III) precursors. For example, $[\{(tpp)Fe\}_2(\mu\text{-}N)]$ was obtained in 83% yield by thermolysis of $[(tpp)Fe^{III}(N_3)]$ which is kinetically a clean first-order decomposition. At that time two possible mechanisms were proposed both of which invoked the formation of $(tpp)Fe^{V}N$ and N_2 as the rate-determining step. Such an intermediate has been characterized by RR spectroscopy where the $Fe^{V}\equiv N$ species was generated by photolysis of $[(tpp)Fe(N_3)]$ in frozen CH_2Cl_2 solution at ≈ 30 K.[47] These $Fe^{V}N$ intermediates are very reactive and are believed to attack the $Fe^{III}(N_3)$ precursor with formation of an $Fe^{V}(N_4)Fe^{III}$ intermediate which decomposes rapidly to give two equivalents of N_2 and two equivalents of an iron(II) species, $[(tpp)Fe^{II}]$. As the concentration of this species builds up the $[(tpp)Fe^{V}N]$ species reacts with it with product formation [Eqs. (10)–(13)].

$$LFe^{III}-N_3 \xrightarrow[\Delta H]{h\nu} LFe^{V}N + N_2 \text{ rate-determining} \qquad (10)$$

$$LFe^{V}N + LFe^{III}(N_3) \longrightarrow LFe^{V}(N_4)Fe^{III}L \qquad (11)$$

$$LFe^{V}(N_4)Fe^{III}L \longrightarrow 2\,LFe^{II} + 2\,N_2 \qquad (12)$$

$$LFe^{V}N + LFe^{II} \longrightarrow LFe^{3.5}(\mu\text{-}N)Fe^{3.5}L \qquad (13)$$

Buchler and Dreher[12] have shown that it is possible to intercept and scavenge the proposed LFe^{II} intermediate by carrying out the above reaction in a coordinating solvent mixture of tetrahydrofuran/pyridine (py) which generated $[(tpp)Fe^{II}(py)_2]$ in 50% yield *without* detectable formation of $[(tpp)_2Fe_2(\mu\text{-}N)]$. This result might suggest that direct formation of $[(tpp)Fe^{II}]$ by photolytic homolysis of the Fe^{III}–N_3 bond as depicted in Equation (14) is also a viable pathway.

$$[(tpp)Fe^{III}(N_3)] \xrightarrow[py]{h\nu} LFe^{II}(py)_2 + 1.5\,N_2 \qquad (14)$$

Note that in the above mechanistic reaction sequence, the iron(II) formation is dependent on the efficiency of Fe^{V}–N production, whereas in the mechanism depicted in Equation (14), it is not. Interestingly, Ercolani et al.[16a] report the synthesis of the asymmetrically coordinated species $[(tpp)Fe^{3.5}(\mu\text{-}N)Fe^{3.5}(pc)]$ in 65% yield from the thermal reaction of $[(tpp)Fe^{III}(N_3)]$ and $[Fe^{II}(pc)]$ in xylene. This result is compatible with the above mechanism since some impurity of $[(tpp)_2Fe_2(\mu\text{-}N)]$ but *not* of $[(pc)_2Fe_2(\mu\text{-}N)]$ has been reported because a $[(pc)Fe^{V}N]$ intermediate cannot form.

0947-6539/99/0502-0806 $ 17.50+.50/0 *Chem. Eur. J.* **1999**, *5*, No. 2

In contrast, the photolysis of an equimolar mixture of **3** and $[L(Cl_4\text{-cat})Fe^{III}(N_3)]$ produces **8** in ≈50% yield. $[\{L(Ph_2acac)Fe\}_2(\mu\text{-}N)]^{2+}$ *and* **9** have *not* been detected as products in this reaction. Both would have been expected to form if the dinuclear intermediates $Fe^{V}(N_4)Fe^{III}$ were the only source of the necessary Fe^{II}. Therefore, we propose that under photolysis conditions using a Hg immersion lamp (220–400 nm) it is very likely that homolysis of the Fe^{III}–N_3 bond occurs generating Fe^{II} and an $N_3\cdot$ radical (which decomposes to N_2), in addition to the formation of $Fe^{V}N$ intermediates [Eq. (15)].

$$L'Fe^{III}\text{-}N_3 \xrightarrow[h\nu]{h\nu} \begin{array}{l} L'Fe^{V}N + N_2 \\ L'Fe^{II} + N_3 (2\,N_3 \rightarrow 3\,N_2) \end{array} \quad (15)$$

We speculate that both processes also occur in a thermal reaction.[48] At least for $[LFe(Ph_2acac)(N_3)]ClO_4$ the quantitative formation of $[LFe^{II}(Ph_2acac)]^+$ has been shown to occur by thermolysis of the former in the solid state. Interestingly, the same thermolysis reaction of $[LFe^{III}(Cl_4\text{-cat})(N_3)]$ does *not* produce $[LFe^{II}(Cl_4\text{-cat})]$. This reactivity difference is probably due to the fact that catecholates stabilize the high-valent iron ion, that is $[LFe^{V}(Cl_4\text{-cat})N]$, but make $[LFe^{II}(Cl_4\text{-cat})]$ quite difficult to access. In comparison, for coordinated acetonylacetates the Fe^{II} oxidation state is more readily accessible and Fe^{V} is more difficult to generate. These observations can—at least in part—explain why the above reaction produces $[L(Ph_2acac)Fe^{III}(\mu\text{-}N)Fe^{IV}(Cl_4\text{-cat})L]^+$ as the only isolable dinuclear product. We emphasize that the exact mechanism of formation of complexes containing the $[Fe(\mu\text{-}N)Fe]^{4+}$ core from Fe^{III}–N_3 precursors by thermolysis or photolysis is still far from being understood.

We now discuss some structural and magnetochemical aspects of binuclear complexes containing the $[Fe^{III}(\mu\text{-}O)Fe^{III}]^{4+}$ core. Complexes **4** and **5** of this work and previously structurally characterized species **10**,[10] $[\{L(Ph_2acac)_2Fe^{III}\}_2(\mu\text{-}O)](ClO_4)_2$,[23] and the asymmetric species $[L(Cl_4\text{-cat})Fe^{III}(\mu\text{-}O)Fe^{III}(Ph_2acac)L]\,BPh_4$[23] contain two octahedral high-spin ferric ions which are connected by an oxo bridge (corner-sharing bioctahedral). The asymmetric species is the exact analogue of complex **8**. It is therefore noteworthy that the Fe–O_b bond lengths are not equivalent in the $\{LFe^{III}(Ph_2acac)O\}$ half (1.787(3) Å) and in the $\{LFe(Cl_4\text{-cat})O\}$ half (1.825(3) Å) of the monocation ($\Delta = 0.038$ Å); the Fe-O-Fe bond angle is 173.7(2)°. This bond length difference is a consequence of the differing π-donor strength of a coordinated catecholate versus an acetonylacetonate which is stronger for the former and weaker for the latter.

The strength of the intramolecular antiferromagnetic exchange coupling as expressed by the coupling constant J using the spin Hamiltonian $H = -2J S_1 S_2$ ($S_1 = S_2 = 5/2$) is known to depend primarily on the average Fe–O_b bond length R. Gorun and Lippard[39] have ignored a correlation of J with the bridging Fe-O-Fe angle Φ and have derived Equation (16) from a statistical analysis of data.

$$-J_{GL} = 8.763 \times 10^{11} \exp(-12.663 \times R) \quad (16)$$

On the other hand, Weihe and Güdel[40] have recently derived a similar equation [Eq. (17)] which correlates J with R *and* Φ.

$$-J_{WG} = 0.6685 \times 10^{8}\,(3.536 + 2.488\cos\Phi + \cos^2\Phi) \times \exp(-7.909R) \quad (17)$$

In Table 7 we have compiled structural and magnetochemical data of seven similar complexes where the Fe–O_b distance spans the range 1.787(5) to 1.811(1) Å and the angle Φ is in the large range of 180 to 120°; the measured J values range from −90 to −122 cm^{-1}. We have calculated J_{GL} values according to the Gorun/Lippard model and J_{WG} values according to the Güdel/Weihe model (Table 7, columns 3 and 4). Inspection of these data reveals that J_{GL} values are nearly consistently larger than the observed values and J_{WG} values are too small. Complexes **10** and $[\{LFe^{III}\}_2(\mu\text{-}O)(\mu\text{-}CH_3CO_2)_2]PF_6$ have the same Fe – O_b distance within experimental error at 1.802 Å but the Fe-O-Fe angles Φ differ by ≈60°. The experimental J values differ by 24 cm^{-1} which is about half the predicted value by the Weihe/Güdel model. The antiferromagnetic coupling in complexes containing the $[Fe^{III}(\mu\text{-}N)Fe^{IV}]^{4+}$ core with an $S_t = 3/2$ ground state, namely **6**, **8**, and **9**, is significantly stronger than in $[Fe^{III}(\mu\text{-}O)Fe^{III}]^{4+}$ species. From the above MO calculations it follows that this coupling is approximately one order of magnitude larger. This is due to a significantly increased covalency of the Fe–N_b bonds as compared to the corresponding Fe–O_b bonds. The $S_t = 3/2$ ground state is attained by coupling of a high-spin Fe^{III} (d^5, $S = 5/2$) with a Fe^{IV} (d^4, $S = 1$) ion. In contrast, in complexes containing an $[Fe^{3.5}(\mu\text{-}N)Fe^{3.5}]^{4+}$ ($S_t = 1/2$) core, a low-spin Fe^{III} (d^5, $S = 1/2$) is very strongly antiferromagnetically coupled to an Fe^{IV} (d^4, $S = 1$) ion.

The degree of delocalization of the excess electron in the $[Fe(\mu\text{-}N)Fe]^{4+}$ species with $S_t = 3/2$ and $S_t = 1/2$ varies; in the former the valencies are nearly trapped (class II), whereas in the latter they are fully delocalized (class III). This can be viewed as a consequence of the larger Franck–Condon barrier to intramolecular electron transfer in the $S_t = 3/2$ as compared to the $S_t = 1/2$ species. The Fe–X bond lengths in an octahedral low-spin Fe^{III} and an Fe^{IV} (d^4, $S = 1$) ion are similar whereas they differ significantly in octahedral high-spin Fe^{III} where the antibonding e_g^* orbitals are half-occupied and the Fe^{IV} (d^4, $S = 1$) ion with empty e_g^*. This is also reflected by the ionic radii of octahedral iron ions: high-spin Fe^{III} (0.785 Å) > low-spin Fe^{III} (0.69 Å) ≈ low-spin Fe^{IV}.

Experimental Section

Synthesis of complexes: The following preparations of complexes have been described previously: $[LFe^{III}Cl_3]$,[49] $[LFe^{III}(Cl_4\text{-cat})(N_3)]$,[10] $[\{L(Cl_4\text{-cat})Fe^{III}\}_2(\mu\text{-}O)]$,[10] $[\{L(Cl_4\text{-cat})Fe\}_2(\mu\text{-}N)]$,[10] $[\{L(Cl_4\text{-cat})Fe^{IV}\}_2(\mu\text{-}N)]Br$,[10] and $[LFe^{II}(Cl_4\text{-cat})(NCCH_3)]2H_2O$.[10]

[LFe(nadiol)Cl] (**1**): Naphthaline-2,3-diol (nadiolH_2) (0.18 g, 1.14 mmol) and sodium methanolate (0.125 g, 2.28 mmol) were added to a suspension of $[LFeCl_3]$ (0.30 g, 0.90 mmol) in dry methanol (30 mL). The mixture was heated to reflux for 4 h until a clear deep-blue solution was obtained which was then cooled to −25 °C. Within a few hours a deep violet microcrystalline material precipitated which was collected by filtration and recrystallized from an acetone:toluene (1:1 (v/v)) mixture. Yield: 0.28 g (73%). MS (FAB) (MNBA): m/z (%): 420 [M^+], 385 [{M − Cl}$^+$], 262 [{M − nadiol}$^+$]; elemental analysis calcd for $C_{19}H_{27}ClFeN_3O_2$ (%): C 54.2, H 6.5, N 10.0, Cl 8.4, Fe 13.3; found: C 54.0, H 6.7, N 9.8, Cl 8.9, Fe 13.1.

[LFe(nadiol)(N_3)] (**2**): Sodium azide (2.0 g, 31 mmol) was added to a blue solution of **1** (0.80 g, 1.90 mmol) in dry acetone (60 mL) and heated

to reflux for 18 h. Upon cooling to 5 °C, blue-grey crystals of **2** precipitated which were collected by filtration, and washed with water and a small amount of ethanol in order to remove impurities of NaN_3 and **5**, respectively. Yield: 0.60 g (74 %). MS (FAB) (MNBA): *m*/*z* (%): 427 [M^+], 385 [{M – Cl}$^+$]; elemental analysis calcd for $C_{19}H_{27}FeN_6O_2$ (%): C 53.4, H 6.4, N 19.7, Fe 13.1; found: C 52.9, H 6.5, N 19.3, Fe 12.8.

[LFe(Ph$_2$acac)(N$_3$)]ClO$_4$ (**3**): [$LFeCl_3$] (1.0 g, 3.0 mmol) was added to a suspension of K[Ph_2acac] (1.0 g, 3.8 mmol) and NaN_3 (0.50 g, 7.7 mmol) in CH_3CN (80 mL). A rapid color change to deep red was observed and a deep red microcrystalline precipitate formed. A few drops of $HClO_4$ (60 %) were added to the suspension of until a clear solution was obtained. A solution of $NaClO_4$ (1.0 g) in water (20 mL) was added whereupon deep red microcrystalline **3** precipitated within a few days. Recrystallization from a CH_3CN:H_2O (1:1) mixture. Yield: 1.3 g (73 %). Elemental analysis calcd for $C_{24}H_{32}N_6O_6ClFe$ (%): C 48.7, H 5.45, N 14.2; found: C 48.3, H 5.2, N 14.1.

The corresponding tetraphenylborate salt, [LFe(Ph_2acac)(N_3)]BPh_4, was obtained from an acetone solution of **3** by addition of Na(BPh_4) (slight excess).

[{LFe^{III}(acac)}$_2$(μ-O)](ClO$_4$)$_2$ (**4**): A solution of 1,4,7-trimethyl-1,4,7-triazacyclononane (0.40 g, 2.3 mmol) in methanol (10 mL) was added to a solution of [Fe(acac)$_3$] (0.80 g, 2.3 mmol) in acetone (20 mL). After heating the mixture to reflux for 30 min, $NaClO_4$ (0.5 g) dissolved in water (5 mL) was added. Yellow-brown crystals of **4** precipitated from the red solution overnight which were recrystallized from an acetone:toluene (1:1) mixture as **4**·toluene. Yield: 1.5 g (75 %). MS (FAB) (MNBA): *m*/*z* (%): 767(5) [{*M*+ClO_4}$^+$], 668(23) [M^+]; elemental analysis calcd for $C_{28}H_{56}N_6Cl_2O_{13}Fe_2$(%): C 38.8, H 6.5, N 9.7, Cl 8.2; found: C 38.6, H 6.6, N 9.5, Cl 8.8.

[{LFe^{III}(nadiol)}$_2$(μ-O)]2mesitylene·2H$_2$O (**5**): Aqueous 0.10 M NaOH (10 mL) was added to a solution of **1** (0.40 g, 0.95 mmol) in acetone (50 mL). After stirring for 10 h at ambient temperature, the solution was filtered to remove FeO(OH). The solution was allowed to stand in an open vessel until red-brown crystals of **5** had precipitated which were collected by filtration, washed with H_2O and ice-cold ethanol and dry diethyl ether. Yield: 0.35 g (74 %). Crystals suitable for X-ray crystallography were grown from an acetone:mesitylene (1:1) mixture: [{LFe(nadiol)}$_2$(μ-O)]·2mesitylene·2H_2O. MS (FAB) (MNBA): *m*/*z* (%): 786 [M^+], 385 [{LFe(nadiol)}$^+$]; elemental analysis calcd for $C_{52}H_{70}Fe_2N_6O_5$ (%): C 64.3, H 7.3, N 8.7, Fe 11.5; found: C 63.7, H 7.6, N 8.9, Fe 11.7.

[{LFe(nadiol)}$_2$(μ-N)]·2toluene (**6**): A blue solution of **2** (0.15 g, 0.35 mmol) in dry, deaerated CH_3CN (200 mL) was photolyzed at room temperature for 8 h with a quartz Hg-immersion lamp. During this process, a constant stream of argon was passed through the solution. During photolysis, the color of the solution changed gradually from blue to deep brown. The solvent was removed by rotary evaporation and the residue was dissolved in a mixture of dry acetone:toluene (1:1) (30 mL). The volume of the filtered solution was reduced by rotary evaporation by one half. Within one to two days red-brown crystals of **6** precipitated from this solution. Yield: 0.07 g (41 %). MS (FAB) (MNBA): *m*/*z* (%): 784.4 [M^+], 385 [{LFe(nadiol)}$^+$]; elemental analysis calcd for $C_{52}H_{70}Fe_2N_7O_4$ (%): C 64.5, H 7.3, N 10.1, Fe 11.5; found: C 65.0, H 7.4, N 10.0, Fe 11.2.

[{LFe(nadiol)}$_2$(μ-N)]PF$_6$·toluene (**7**): Ferrocenium hexafluorophosphate (0.07 g, 0.21 mmol) was added to a deaerated solution of **6** (0.20 g, 0.21 mmol) in dry CH_2Cl (40 mL) with stirring. After 18 h of continuous stirring at 20 °C, a blue precipitate formed which was collected by filtration and washed repeatedly with small portions of diethyl ether. The residue was dissolved in dry CH_3CN and purified by column chromatography (Al_2O_3) with CH_3CN. To the resulting solution, an equivalent amount of toluene was added. Within a few days cubic crystals suitable for X-ray crystallography grew from this solution. Yield: 0.05 g (23 %). MS (FAB) (MNBA): *m*/*z* (%): 784.2 [M^+]; elemental analysis calcd for $C_{45}H_{62}F_6Fe_2N_7O_4P$ (%): C 52.9, H 6.1, N 9.6, Fe 10.9; found: C 53.0, H 6.1, N 9.6, Fe 10.7; ^{1}H NMR (400 MHz, CD_3NO_2): δ = 2.04 (3H, s, N-CH_3), 2.28 (1.5H, s, toluene), 2.34 – 2.42 (2H, m, CH_2), 2.46 – 2.57 (4H, m, CH_2), 2.60 – 2.66 (2H, m, CH_2), 2.70 – 2.77 (2H, m, CH_2), 2.99 – 3.05 (2H, m, CH_2), 3.5 (6H, s, N-CH_3), 6.99 – 7.01 (2H, AA′ part of AA′XX′ system of aromatic protons), 7.03 (2H, s, aromatic protons), 7.08 – 7.23 (2.5H, m, toluene), 7.44 – 7.46 (2H, XX′ part of AA′XX′ system).

[L(Ph$_2$acac)Fe(μ-N)Fe(Cl$_4$-cat)L]ClO$_4$·toluene (**8**): A solution of **3** (0.15 g, 0.25 mmol) and [LFe(Cl_4-cat)(N_3)] (0.15 g, 0.29 mmol) in dry CH_3CN (100 mL) was photolyzed in a quartz tube with a Hg high-pressure lamp for 12 h during which time a constant stream of argon was passed through the solution. A color change to deep brown was observed. Evaporation of the solvent under reduced pressure produced a brown-black residue which was recrystallized three times from a dry acetone:toluene (1:1) mixture. Yield: 0.16 g (52 %) ESI (positive-ion mode): *m*/*z* (%): 937 [M^+]; elemental analysis calcd for $C_{46}H_{61}N_7O_8Cl_5Fe_2$ (%): C 48.9, H 5.45, N 8.7; found: C 48.7, H 5.2, N 8.9.

The corresponding tetraphenylborate salt was prepared from an acetonitrile:ethanol (1:1) mixture of the ClO_4^- salt by addition of $NaBPh_4$. The resulting precipitate was recrystallized from acetonitrile:toluene (1:1).

Physical methods and molecular orbital calculations

Electronic spectra of complexes were recorded on a Perkin-Elmer UV/Vis/NIR Spectrophotometer Lambda 19 in the range 210 – 2000 nm. Cyclic voltammetric and coulometric measurements were performed on EG&G equipment (potentiostat/galvanostat Model 273A). The X-band EPR spectra were recorded on a Bruker ESP 300E spectrometer equipped with a helium-flow cryostat (Oxford Instruments ESR 910). Infrared spectra of complexes were measured on a Perkin-Elmer FT-IR 2000 spectrometer as KBr disks. The magnetic susceptibilities of solid samples of complexes were measured in the temperature range 2 – 300 K with a SQUID-susceptometer (MPMS Quantum Design) with an external field of 1.0 T. The raw data were corrected by underlying diamagnetism by use of Pascal tabulated constants. The Mössbauer spectra were recorded on an alternating constant-acceleration spectrometer. The minimal experimental line-width was 0.24 mm s^{-1} full-width at half-height. The sample temperature was maintained constant either in an Oxford Variox or an Oxford Mössbauer-Spectromag cryostat. The latter is a split-pair superconducting magnet system for applied fields up to 8 T where the temperature of the samples can be varied in the range 1.5 to 250 K. The field at the sample is oriented perpendicular to the γ-beam. The ^{57}Co/Rh source (1.8 GBq) was positioned at room temperature inside the gap of the magnet system at a zero-field position. Isomer shifts are referenced relative to iron metal at 295 K.

Resonance Raman (RR) spectra were recorded with a double monochromator (2400/ mm holographic gratings, Spex Inc.) equipped with a photon counting system. The output of a krypton ion laser (Spectra Physics) served as excitation sources. The laser power at the sample was about 50 mW. In order to avoid photoinduced degradation, the sample, which exhibits an optical density of about 1.5 at the excitation wavelength, was deposited in a rotating cell. The Raman scattered light was detected at 90° with a scrambler placed in front of the entrance slit of the spectrometer to account for the polarization sensitivity of the gratings. The spectral slit width was 2.8 cm^{-1} and the wavenumber increment was 0.2 cm^{-1} per data point. Up to 15 individual scans were added to improve the signal-to-noise ratio. Thus, the total accumulation time was about 15 s per data point. In the spectra shown in this work, the contributions from the solvent were subtracted. Molecular orbital (MO) calculations were carried out in local density approximation (LDA)[50, 51] by the spin-polarized self-consistent-charge (SCC)Xα method.[52–54] The Mössbauer parameters, namely the isomer shift and the quadrupole splitting have been calculated as described in detail previously.[55] The measured quadrupole splitting ΔE_Q is related to the components $|V_{zz}| \geq |V_{xx}| \geq |V_{yy}|$ of the electric field gradient (efg) tensor in its principal axes system [Eq. (18)], with the asymmetry parameter $\eta = |V_{xx} - V_{yy}| / |V_{zz}|$ and the nuclear quadrupole moment $Q = 0.15$ barn.[56]

$$\Delta E_Q = (\tfrac{1}{2})eQV_{zz}(1 + \eta^2/3)^{1/2} \quad (18)$$

Core polarization effects are taken into account by the Sternheimer shielding function γ(r) derived from atomic self-consistent first-order perturbation calculations.[57] Apart from these approximations, the efg tensor is computed rigorously within the frame of a valence-electron-only MO method.[55] The isotropic Heisenberg exchange coupling constant *J* in the Heisenberg Hamiltonian $H = -2JS_iS_j$ is derived within the broken-symmetry formalism[58] [Eq. (19)], where E(S_{max}) and E(S_{min}) are the SCC-Xα total energies of the state with maximum spin and the state with broken-symmetry, respectively.

0947-6539/99/0502-0808 $ 17.50+.50/0 *Chem. Eur. J.* **1999**, *5*, No. 2

$$J = [E(S_{min}) - E(S_{max})]/[S^2_{max} - S^2_{min}] \quad (19)$$

X-ray crystallography: A brown single crystal of **4**, and black crystals of **5**, **6**, **7**, and **8** were mounted in glass capillaries sealed under argon. Graphite-monochromated $Mo_{K\alpha}$ radiation ($\lambda = 0.71073$ Å) was used throughout. Crystallographic data of the compounds and diffractometer types used are listed in Table 12. Cell constants for **4**, **5**, **6**, and **7** were obtained from a least-square fit of the setting angles of 25 carefully centered reflections. Their data were collected at 20(1) °C using the ω-2θ scan technique, corrected for Lorentz and polarization effects but no absorption correction was carried out due to small absorption coefficients. Compound **8** was measured on a Siemens SMART CCD-detector system equipped with a cryogenic cold stream at 100(2) K. Cell constants were obtained from a subset of 6827 strong reflections. Data collection was performed by a hemisphere run taking frames at 0.30° in ω. A semiempirical absorption correction using the program SADABS (G.M. Sheldrick, Universität Göttingen) afforded minimum and maximum transmission factors of 0.537 and 0.903, respectively.

The Siemens SHELXTL V.5 software package (Siemens Analytical X-ray Instruments, Inc. 1994) was used for solution, refinement and artwork of the structures. All structures were readily solved and refined by direct methods and difference Fourier techniques performed on DEC Alpha workstations. All non-hydrogen atoms were refined anisotropically except those of the disordered parts of the macrocycle and solvent molecules which were isotropically refined by split-atom models. All hydrogen atoms were placed at calculated positions and refined as riding atoms with isotropic displacement parameters.

Ethylene groups in the macrocycles coordinated to Fe(1) in **4** and **8** showed disproportionate large displacement parameters leading to unrealistically short C–C distances due to disorder problems imposed by crystallographic symmetry. An isotropic split atom model with a 1:1 occupancy of the methylene carbon atoms was applied yielding the expected λλλ- and δδδ-conformation of the coordinated macrocycle. Hydrogen atoms of these methylene carbon atoms were attached geometrically with an occupancy factor of 0.5. Complexes **5**, **6**, and **7** also showed slight torsional disorder of the methylene carbons but splitting of atoms did not improve the structure quality. Perchlorate anions in **4** were found to be disordered and a split atom model was applied satisfactorily yielding two positions with a 0.5 occupancy for each of oxygen atoms.

Crystals of **4**, **6**, and **7** contain toluene solvent molecules, while **5** crystallizes with mesitylene and water. Attempts to localize the hydrogen atoms of the water molecule failed. All organic solvent molecules were poorly defined and disordered. A 1:1 split-atom model was used for the methyl group of toluene in **4** lying on a center of inversion. The methyl group of toluene in crystals of **7** could not be located and therefore was not included in the refinement. Crystallographic data (excluding structure factors) for the structures reported in this paper have been deposited at the Cambridge Crystallographic Data Centre as supplementary publication no. CCDC-101 181. Copies of the data can be obtained free of charge on application to CCDC, 12 Union Road, Cambridge CB2 IEZ, UK (fax: (+44) 1223-336-033; e-mail: deposit@ccdc.cam.ac.uk).

Acknowledgements

We thank the Fonds der Chemischen Industrie for financial support of this work.

[1] J. Sanders-Loehr, *Iron Carriers and Iron Proteins* (Ed.: T. M. Loehr), VCH, New York, **1989**, p. 375.
[2] a) D. M. Kurtz, *Chem. Rev.* **1990**, *90*, 585; b) L. Que, Jr., A. E. True, *Progr. Inorg. Chem.* **1990**, *38*, 97; c) S. J. Lippard, *Angew. Chem.* **1988**, *100*, 353; *Angew. Chem. Int. Ed. Engl.* **1988**, *27*, 344; d) J. B. Vincent, G. L. Olivier-Lilley, B. A. Averill, *Chem. Rev.* **1990**, *90*, 1447.
[3] a) K. K. Andersson, A. Gräslund, *Adv. Inorg. Chem.* **1995**, *43*, 359; b) S. Eriksson, B.-M. Sjöberg, *Allosteric Enzymes* (Ed.: G. Hervé) CRC Press Inc., Boca Raton, FL, 1989, p. 189; c) J. Stubbe, *Adv. Enzymol.* **1990**, *63*, 349.
[4] a) K. E. Liu, S. J. Lippard, *Adv. Inorg. Chem.* **1995**, *42*, 263; b) B. J. Wallar, J. D. Lipscomb, *Chem. Rev.* **1996**, *96*, 2625.
[5] a) A. L. Feig, S. J. Lippard, *Chem. Rev.* **1994**, *94*, 759; b) D. E. Edmondson, B. H. Huynh, *Inorg. Chim. Acta* **1996**, *252*, 399.
[6] a) L. Que Jr., Y. Doug, *Acc. Chem. Res.* **1996**, *29*, 190; b) L. Shu, J. C. Nesheim, K. Kauffmann, E. Münck, J. D. Lipscomb, L. Que Jr., *Science* **1997**, *275*, 515.
[7] Y. Doug, H. Fujii, M. P. Hendrich, R. A. Leising, G. Pan, C. R. Randall, E. C. Wilkinson, Y. Zang, L. Que Jr., B. G. Fox, K. Kauffmann, E. Münck, *J. Am. Chem. Soc.* **1995**, *117*, 2778.
[8] Y. Doug, L. Que Jr., K. Kauffmann, E. Münck, *J. Am. Chem. Soc.* **1995**, *117*, 11 377.
[9] a) C. Kim, Y. Doug, L. Que Jr., *J. Am. Chem. Soc.* **1997**, *119*, 3635; b) J. Kim, R. G. Harrison, C. Kim, L. Que Jr., *J. Am. Chem. Soc.* **1996**, *118*, 4373.
[10] T. Jüstel, T. Weyhermüller, K. Wieghardt, E. Bill, M. Lengen, A. X. Trautwein, P. Hildebrandt, *Angew. Chem.* **1995**, *107*, 744; *Angew. Chem. Int. Ed. Engl.* **1995**, *34*, 669.
[11] D. A. Summerville, I. A. Cohen, *J. Am. Chem. Soc.* **1976**, *98*, 1747.
[12] J. W. Buchler, C. Dreher, *Z. Naturforsch. B.* **1984**, *39*, 222.
[13] W. R. Scheidt, D. A. Summerville, I. A. Cohen, *J. Am. Chem. Soc.* **1976**, *98*, 6623.

Table 12. Crystallographic data for **4** · toluene, **5** · 2 mesitylene · 2 H_2O, **6** · 2 toluene, **7** · toluene, and **8.**

	4 · toluene	**5** · 2 mesitylene · 2 H_2O	**6** · 2 toluene	**7** · toluene	**8** · toluene
formula	$C_{35}H_{64}Cl_2Fe_2N_6O_{13}$	$C_{56}H_{82}Fe_2N_6O_7$	$C_{52}H_{70}Fe_2N_7O_4$	$C_{45}H_{62}F_6Fe_2N_7O_4P$	$C_{46}H_{61}Cl_5Fe_2N_7O_8$
fw [g mol^{-1}]	959.52	1062.98	968.86	1021.69	1128.97
space group	$P4_2/mbc$	$P2_1/n$	$P2_1/n$	$C2/c$	$P2_1/n$
a [Å]	16.462(2)	11.167(6)	10.863(3)	29.006(8)	16.292(3)
b [Å]	13.802(7)	13.425(4)	13.162(5)	13.801(3)	
c [Å]	16.764(3)	18.370(10)	16.718(5)	13.179(5)	22.849(5)
β [°]	100.37(5)	93.24(2)	113.94(3)	100.57(3)	
V [Å^3]	4543(1)	2785(3)	2434(1)	4599(3)	5050(7)
T [K]	293	293	293	293	100
Z	4	2	2	4	4
diffractometer	Siemens P4	Siemens P4	AED	SYNTEX R3	Siemens SMART
ρ_{calcd} [g cm^{-3}]	1.403	1.268	1.322	1.476	1.485
no. of data	1537	2745	1956	3508	21658
obs. unique data	1537	2745	1881	3231	6547
no. of parameters	158	322	283	277	569
$\mu Mo_{K\alpha}$ [cm^{-1}]	8.20	5.76	6.48	7.41	8.98
$R1$[a]	0.0685	0.0509	0.0821	0.0733	0.0725
$wR2$[b]	0.1529	0.1236	0.1621	0.1693	0.1580

[a] Observation criterion $I > 2\sigma(I)$, $R1 = \Sigma ||F_o| - |F_c|| / \Sigma |F_o|$, $R_w = [\Sigma w(|F_o| - |F_c|)^2/(wF_o^2)]^{1/2}$ where $w = 4F_o^2/\sigma^2(F_o^2)$. [b] $wR2 = [\Sigma[w(F_o^2 - F_c^2)^2]/\Sigma[w(F_o^2)^{2-}]^{1/2}$ where $w = 1/\sigma^2(F_o^2) + (aP)^2 + bP$, $P = (F_o^2 + 2F_c^2)/3$.

[14] a) L. A. Bottomley, B. B. Garrett, *Inorg. Chem.* **1982**, *21*, 1260; b) G. A. Schick, E. W. Findsen, D. F. Bocian, *Inorg. Chem.* **1982**, *21*, 2885; c) K. M. Kadish, L. A. Bottomley, J. G. Brace, N. Winograd, *J. Am. Chem. Soc.* **1980**, *102*, 4341; d) K. Tatsumi, R. Hoffmann, *J. Am. Chem. Soc.* **1981**, *103*, 3328.
[15] a) V. L. Goedken, C. Ercolani, *J. Chem. Soc. Chem. Commun.* **1984**, 378; b) L. A. Bottomley, J.-N. Gorce, V. L. Goedken, C. Ercolani, *Inorg. Chem.* **1985**, *24*, 3733; c) B. J. Kennedy, K. S. Murray, H. Homborg, W. Kalz, *Inorg. Chim. Acta* **1987**, *134*, 19; d) C. Ercolani, M. Gardini, G. Pennesi, G. Rossi, U. Russo, *Inorg. Chem.* **1988**, *27*, 422.
[16] a) C. Ercolani, S. Hewage, R. Heucher, G. Rossi, *Inorg. Chem.* **1993**, *32*, 2975; b) C. Ercolani, J. Jubb, G. Pennesi, U. Russo, G. Trigiante, *Inorg. Chem.* **1995**, *34*, 2535.
[17] M. B. Robin, P. Day, *Adv. Inorg. Chem. Radiochem.* **1967**, *10*, 247.
[18] a) D. R. English, D. N. Hendrickson, K. S. Suslick, *Inorg. Chem.* **1985**, *24*, 122; b) B. Moubaraki, D. Benlian, A. Baldy, M. Pierrot, *Acta Crystallogr. C* **1989**, *45*, 393.
[19] a) S. H. Strauss, M. J. Pawlik, J. Skowyra, J. R. Kennedy, O. P. Anderson, K. Spartalian, J. L. Dye, *Inorg. Chem.* **1987**, *26*, 724; b) I. A. Cohen, *J. Am. Chem. Soc.* **1969**, *91*, 1980; c) E. B. Fleischer, T. S. Srivastava, *J. Am. Chem. Soc.* **1969**, *91*, 2403.
[20] a) C. Ercolani, G. Rossi, F. Monacelli, *Inorg. Chim. Acta* **1980**, *44*, L215; b) C. Ercolani, M. Gardini, F. Monacelli, G. Pennesi, G. Rossi, *Inorg. Chem.* **1983**, *22*, 2584.
[21] a) E. Vogel, S. Will, A. Schulze-Tilling, L. Neumann, J. Lex, E. Bill, A. X. Trautwein, K. Wieghardt, *Angew. Chem.* **1994**, *106*, 771; *Angew. Chem. Int. Ed. Engl.* **1994**, *33*, 731; b) M. Lausmann, I. Zimmer, J. Lex, H. Lueken, K. Wieghardt, E. Vogel, *Angew. Chem.* **1994**, *106*, 776; *Angew. Chem. Int. Ed. Engl.* **1994**, *33*, 736.
[22] V. M. Leovac, R. Herak, B. Prelesnik, S. Niketic, *J. Chem. Soc. Dalton Trans.* **1991**, 2295.
[23] M. Müller, T. Weyhermüller, E. Bill, K. Wieghardt, *J. Biol. Inorg. Chem.* **1998**, *3*, 96.
[24] R. S. Czernuszewicz, W.-D. Wagner, G. B. Ray, K. Nakamoto, *J. Mol. Struct.* **1991**, *242*, 99.
[25] K. M. Adams, P. G. Rasmussen, W. R. Scheidt, K. Hatano, *Inorg. Chem.* **1979**, *18*, 1892.
[26] M. Müller, E. Bill, T. Weyhermüller, K. Wieghardt, *J. Chem. Soc. Chem. Commun.* **1997**, 705.
[27] K. Wieghardt, K. Pohl, U. Bossek, *Z. Naturforsch. B* **1988**, *43*, 1184.
[28] J. Sanders-Loehr, W. D. Wheeler, A. K. Shiemke, B. A. Averill, T. M. Loehr, *J. Am. Chem. Soc.* **1989**, *111*, 8084.
[29] a) R. C. Reem, J. M. McCormick, D. E. Richardson, F. J. Devlin, P. J. Stephens, R. L. Musselman, E. I. Solomon, *J. Am. Chem. Soc.* **1989**, *111*, 4688; b) C. A. Brown, G. J. Remar, R. L. Musselman, E. I. Solomon, *Inorg. Chem.* **1995**, *34*, 688.
[30] M. A. Crisanti, T. G. Spiro, D. R. English, D. N. Hendrickson, K. S. Suslick, *Inorg. Chem.* **1984**, *23*, 3897.
[31] A. Kienast, C. Bruhn, H. Homborg, *Z. Anorg. Allg. Chem.* **1997**, *623*, 967.
[32] G. Rossi, V. L. Goedken, C. Ercolani, *J. Chem. Soc. Chem. Commun.* **1988**, 46.
[33] J. M. Burke, J. R. Kincaid, T. G. Spiro, *J. Am. Chem. Soc.* **1978**, *100*, 6077.
[34] G. A. Schick, D. F. Bocian, *J. Am. Chem. Soc.* **1983**, *105*, 1830.
[35] A. X. Trautwein, E. Bill, E. L. Bominaar, H. Winkler, *Struct. Bond* 78, 1–95, Springer Berlin, Heidelberg, 1991.
[36] H. Paulsen, M. Müther, M. Grodzicki, A. X. Trautwein, E. Bill, *Bull. Soc. Chim. Fr.* **1996**, *133*, 703.
[37] K. S. Murray, *Coord. Chem. Rev.* **1974**, *12*, 1.
[38] J. A. Hartman, R. L. Rardin, P. Chaudhuri, K. Pohl, K. Wieghardt, B. Nuber, J. Weiss, G. C. Papaefthymiou, R. B. Frankel, S. J. Lippard, *J. Am. Chem. Soc.* **1987**, *109*, 7387.
[39] S. Gorun, S. J. Lippard, *Inorg. Chem.* **1991**, *30*, 1625.
[40] H. Weihe, H. U. Güdel, *J. Am. Chem. Soc.* **1997**, *119*, 6539.
[41] D. R. English, D. N. Hendrickson, K. S. Suslick, *Inorg. Chem.* **1988**, *22*, 367.
[42] P. Gütlich, R. Link, A. X. Trautwein, *Mössbauer Spectroscopy and Transition Metal Chemistry*, Springer, Berlin, Heidelberg, **1978**.
[43] H. Paulsen, X.-Q. Ding, M. Grodzicki, Ch. Butzlaff, A. X. Trautwein, R. Hartung, K. Wieghardt, *Chem. Phys.* **1994**, *184*, 149.
[44] R. S. Drago, *Physical Methods in Chemistry*, W. B. Saunders, Philadelphia, **1977**, Chap. 9.
[45] M. Grodzicki, unpublished results.
[46] M. Grodzicki, *Croat. Chem. Acta* **1987**, *60*, 263.
[47] W.-D. Wagner, K. Nakamoto, *J. Am. Chem. Soc.* **1989**, *111*, 1590.
[48] For instance, photolysis at 440–750 nm (and γ-irradiation) of $[(tpp)Mn^{III}(N_3)]$ has been shown to produce $[Mn^{II}(tpp)]$ and $[Mn^{V}(tpp)N]$: T. Jin, T. Suzuki, T. Imamura, M. Fujimoto, *Inorg. Chem.* **1987**, *26*, 1280.
[49] K. Wieghardt, K. Pohl, D. Ventur, *Angew. Chem.* **1985**, *97*, 415; *Angew. Chem. Int. Ed. Engl.* **1985**, *24*, 392.
[50] R. G. Parr, W. Yang, *Density Functional Theory of Atoms and Molecules*, Oxford University Press, New York, 1989.
[51] *Local Density Approximations in Quantum Chemistry and Solid State Physics* (Eds.: J. P. Dahl, J. Avery), Plenum, New York and London, **1984**.
[52] M. Grodzicki, *J. Phys. B* **1980**, *13*, 2683.
[53] M. Grodzicki, *Theorie und Anwendung der Self-Consistent-Charge-Xα Methode,* Thesis or Habilitation, Hamburg, 1985.
[54] R. Bläs, J. Guillin, E. L. Bominaar, M. Grodzicki, V. R. Marathe, A. X. Trautwein, *J. Phys. B* **1987**, *20*, 5627.
[55] M. Grodzicki, V. Männing, A. X. Trautwein, J. M. Friedt, *J. Phys. B* **1987**, *20*, 5595.
[56] E. L. Bominaar, J. Guillin, A. Sawaryn, A. X. Trautwein, *Phys. Rev. B* **1989**, *39*, 72.
[57] S. Lauer, V. R. Marathe, A. X. Trautwein, *Phys. Rev. A* **1979**, *19*, 1852.
[58] L. Noodleman, *J. Chem. Phys.* **1981**, *74*, 5737.

Received: May 11, 1998
Revised version: September 11, 1998 [F 1152]

0947-6539/99/0502-0810 $ 17.50+.50/0